The Development of the North Pacific Jet Phase Diagram as an Objective Tool to Monitor the State of the Upper-Tropospheric Flow Pattern

By

ANDREW C. WINTERS[1*], DANIEL KEYSER[1], and LANCE F. BOSART[1]

[1]Department of Atmospheric and Environmental Sciences
University at Albany, State University of New York
Albany, NY 12222

Submitted for publication in *Weather and Forecasting*
21 June 2018

[*] *Corresponding author address:* Andrew C. Winters, Dept. of Atmospheric and Environmental Sciences, University at Albany, SUNY, 1400 Washington Ave., Albany, NY 12222. E-mail: acwinters@albany.edu

ABSTRACT

Previous studies employing empirical orthogonal function (EOF) analyses of upper-tropospheric zonal wind anomalies have identified the leading modes of North Pacific jet (NPJ) variability that prevail on synoptic time scales. The first mode corresponds to a zonal extension or retraction of the exit region of the climatological NPJ, while the second mode corresponds to a poleward or equatorward shift of the exit region of the climatological NPJ. These NPJ regimes can strongly influence the character of the large-scale flow pattern over North America. Consequently, knowledge of the prevailing NPJ regime and the forecast skill associated with each NPJ regime can add considerable value to operational medium-range (6–10-day) forecasts over North America.

This study documents the development of an NPJ Phase Diagram, which is constructed from the two leading EOFs of 250-hPa zonal wind anomalies during 1979–2014 excluding the summer months (Jun–Aug). The projection of 250-hPa zonal wind anomalies at one or multiple times onto the NPJ Phase Diagram provides an objective characterization of the state or evolution of the upper-tropospheric flow pattern over the North Pacific. A 30-year analysis of GEFS reforecasts with respect to the NPJ Phase Diagram demonstrates that forecasts verified during jet retraction and equatorward shift regimes are associated with significantly larger average errors than jet extension and poleward shift regimes. An examination of the best and worst forecasts suggests that periods characterized by rapid NPJ regime transition and the development and maintenance of North Pacific blocking events exhibit reduced forecast skill.

1. Introduction

Anchored downstream of the Asian continent at middle latitudes, the North Pacific jet (NPJ) stream is a narrow, meandering current of strong upper-tropospheric wind speeds bounded by appreciable horizontal and vertical shear. The position and intensity of the NPJ is modulated by a number of external factors, including tropical convection (e.g., Hoskins and Karoly 1981; Madden and Julian 1994; Harr and Dea 2009; Archambault et al. 2013, 2015; Torn and Hakim 2015; Grams and Archambault 2016; Bosart et al. 2017), interactions between the NPJ and baroclinic eddies along the midlatitude storm track (e.g., Orlanski and Sheldon 1995; Chang et al. 2002; Hakim 2003; Torn and Hakim 2015; Bosart et al. 2017), and the East Asian Winter Monsoon (e.g., Jhun and Lee 2004; Lee et al. 2010; Wang and Chen 2014; Handlos and Martin 2016). In combination, these factors contribute to NPJ configurations that vary substantially on both weather and climate time scales.

In an attempt to characterize the variability of the NPJ, prior work has identified the leading modes of NPJ variability that prevail on weather and climate time scales during the winter (Dec–Feb). Schubert and Park (1991) provided one of the first investigations of subseasonal NPJ variability, and calculated the two leading traditional empirical orthogonal functions[1] (EOFs) of 20–70-day filtered zonal wind at 200 hPa over the Pacific basin. Their first EOF describes variability in the intensity of the NPJ over the western North Pacific, while their second EOF describes a zonal extension or retraction of the exit region of the climatological NPJ. In contrast, Eichelberger and Hartmann (2007) employed daily zonal wind data during January in their traditional EOF analysis and found that the first EOF of the vertically averaged zonal-mean zonal wind over the North Pacific encompasses variability in the intensity,

[1] A traditional EOF analysis is a statistical technique to extract patterns that explain the greatest fraction of the variance within a multidimensional dataset (Wilks 2011, Ch. 12).

89 longitudinal extent, and latitudinal position of the NPJ. Consequently, the Eichelberger and
90 Hartmann (2007) analysis suggests that NPJ variability is considerably more complex when
91 analyzed on synoptic rather than subseasonal time scales.

92 Recent studies by Athanasiadis et al. (2010) and Jaffe et al. (2011) provided additional
93 physical clarity on the two leading modes of NPJ variability that prevail on synoptic time scales
94 during the cold season (Nov–Mar). These studies applied traditional EOF analysis to unfiltered
95 upper-tropospheric zonal wind data over the North Pacific and determined that the first mode of
96 NPJ variability corresponds to longitudinal variability in the vicinity of the exit region of the
97 climatological NPJ. Specifically, a positive EOF 1 pattern (+EOF 1) describes a zonal extension
98 of the exit region of the climatological NPJ, while a negative EOF 1 pattern (–EOF 1) describes a
99 zonal retraction of the exit region of the climatological NPJ. The second mode of NPJ variability
100 corresponds to latitudinal variability in the vicinity of the exit region of the climatological NPJ.
101 In the context of this mode, a positive EOF 2 pattern (+EOF 2) describes a poleward shift of the
102 exit region of the climatological NPJ, while a negative EOF 2 pattern (–EOF 2) describes an
103 equatorward shift.

104 Knowledge of the four NPJ configurations identified by Athanasiadis et al. (2010) and
105 Jaffe et al. (2011), hereafter referred to as NPJ regimes, subsequently permits an examination of
106 the relationship between each NPJ regime and the downstream large-scale flow pattern over
107 North America. To this end, Griffin and Martin (2017) employed time-extended EOF analyses
108 (e.g., Weare and Nasstrom 1982; Wilks 2011, Ch. 12) of 250-hPa zonal wind data from the
109 NCEP/NCAR reanalysis dataset (Kalnay et al. 1996) to construct composite analyses of the
110 large-scale flow evolution over the North Pacific and North America during the 10-day period
111 preceding and following the development of each NPJ regime. The Griffin and Martin (2017)

112 analysis yields a clear relationship between each NPJ regime and the large-scale flow pattern
113 over North America, and implies that knowledge of the prevailing NPJ regime may add
114 considerable value to operational medium-range (6–10-day) forecasts of temperature and
115 precipitation over North America. However, this value is limited operationally without
116 complementary knowledge of the relative forecast skill associated with the development or
117 persistence of each NPJ regime.

118 The concept of regime-dependent forecast skill has been explored with respect to large-
119 scale upper-tropospheric flow regimes over the North Atlantic basin (e.g., Ferranti et al. 2015)
120 and with respect to large-scale atmospheric teleconnection patterns (e.g., Palmer 1988; Lin and
121 Derome 1996; Sheng 2002; Ferranti et al. 2015). However, to the authors' knowledge, no study
122 has comprehensively examined regime-dependent forecast skill over the North Pacific with
123 respect to the prevailing NPJ regime. Consequently, a primary goal of the present study is to
124 identify whether certain NPJ regimes exhibit enhanced or reduced forecast skill. In an effort to
125 address this goal, the results from prior studies on NPJ variability (e.g., Athanasiadis et al. 2010;
126 Jaffe et al. 2011; Griffin et al. 2017) are extended to the cool season (Sep–May) and a two-
127 dimensional phase diagram, hereafter referred to as the NPJ Phase Diagram, is developed
128 employing the two leading modes of NPJ variability during that time period. The NPJ Phase
129 Diagram subsequently aids in visualizing the state and evolution of the upper-tropospheric flow
130 pattern over the North Pacific, and serves as an objective tool from which new insights can be
131 derived regarding the climatology and forecast skill of each NPJ regime.

132 The remainder of this manuscript is structured as follows. Section 2 discusses the
133 development of the NPJ Phase Diagram. Section 3 discusses the climatology of each NPJ regime
134 and reviews the large-scale flow patterns associated with each NPJ regime. Section 4 examines

the forecast skill of each NPJ regime with respect to the NPJ Phase Diagram. Section 5 illuminates the characteristics of the best and worst medium-range forecast periods with respect to the NPJ Phase Diagram, and section 6 offers a discussion of the results and some conclusions.

2. Development of the NPJ Phase Diagram

The NPJ Phase Diagram is developed by employing anomalies of the zonal component of the 250-hPa vector wind from the 0.5°-resolution National Centers for Environmental Prediction Climate Forecast System Reanalysis (CFSR; Saha et al. 2010, 2014) at 6-h intervals during 1979–2014 excluding the summer months (Jun–Aug). Anomalies are calculated as the deviation of the instantaneous 250-hPa zonal wind from a 21-day running mean centered on each analysis time in order to remove the 36-year mean as well as the annual and diurnal cycles. The CFSR is chosen for this study because of its role in providing the initial conditions for the Global Ensemble Forecast System (GEFS) Reforecast Version 2 dataset prior to 2011 (Hamill et al. 2013). The GEFS Reforecast dataset is utilized in sections 4 and 5 to examine the forecast skill of each NPJ regime with respect to the NPJ Phase Diagram. A traditional EOF analysis (Wilks 2011, Ch. 12) is subsequently performed on the 250-hPa zonal wind anomaly data within a horizontal domain bounded in latitude from 10°N to 80°N and in longitude from 100°E to 120°W in order to identify the two leading modes of NPJ variability. This horizontal domain is chosen to capture the North Pacific basin and to match the domain employed by Griffin and Martin (2017).

In comparison to traditional EOF analysis, Griffin and Martin (2017) demonstrate that time-extended EOF analysis (e.g., Weare and Nasstrom 1982; Wilks 2011, Ch. 12) of 250-hPa zonal wind anomalies over the North Pacific is beneficial for ensuring that the evolution of the NPJ is characterized by a higher degree of temporal coherence. However, this higher degree of

158 temporal coherence is achieved by filtering out the high-frequency variability of the NPJ that
159 occurs on daily time scales (Griffin and Martin 2017; their Fig. 1). When considering the NPJ
160 and its influence on the downstream upper-tropospheric flow pattern over North America, short-
161 term fluctuations in the position, intensity, and evolution of the NPJ, such as those associated
162 with recurving tropical cyclones or intensifying extratropical cyclones, can have substantial
163 impacts on the character of the downstream upper-tropospheric flow pattern over North America
164 (e.g., Archambault et al. 2015; Torn and Hakim 2015; Grams and Archambault 2016; Bosart et
165 al. 2017). Additionally, the application of time-extended EOF analysis is computationally more
166 expensive than traditional EOF analysis, especially when employing a dataset with 0.5°
167 resolution such as the CFSR. For these two reasons, traditional EOF analysis is chosen for this
168 study. The subsequent analysis demonstrates that the application of traditional EOF analysis to
169 250-hPa zonal wind anomalies during the cool season from the CFSR produces the same two
170 leading modes of NPJ variability as found in previous studies (Athanasiadis et al. 2010; Jaffe et
171 al. 2011; Griffin and Martin 2017).

172 The regression of 250-hPa zonal wind anomalies from the CFSR onto the two leading
173 spatial patterns obtained from the traditional EOF analysis, EOF 1 and EOF 2, are illustrated in
174 Fig. 1. EOF 1 explains 12.2% of the variance of 250-hPa zonal wind over the North Pacific and
175 corresponds to longitudinal variability of the 250-hPa zonal wind in the vicinity of the exit
176 region of the climatological NPJ. A positive EOF 1 pattern (+EOF 1) is associated with a zonal
177 extension of the exit region of the climatological NPJ (i.e., a jet extension), while a negative EOF
178 1 pattern (–EOF 1) is associated with a retraction of the exit region of the climatological NPJ
179 (i.e., a jet retraction). EOF 2 explains 8.8% of the variance of 250-hPa zonal wind over the North
180 Pacific and corresponds to latitudinal variability of the 250-hPa zonal wind in the vicinity of the

exit region of the climatological NPJ. A positive EOF 2 pattern (+EOF 2) is associated with a poleward shift of the exit region of the climatological NPJ (i.e., a poleward shift), while a negative EOF 2 pattern (–EOF 2) is associated with an equatorward shift of the exit region of the climatological NPJ (i.e., an equatorward shift). The combined variance explained by EOF 1 and EOF 2 is comparable to that found in previous studies (Athanasiadis et al. 2010; Jaffe et al. 2011; Griffin and Martin 2017) and the two leading EOFs are statistically well separated using the methodology outlined in North et al. (1982). To ensure that the EOF patterns shown in Fig. 1 are representative of the entire cool season, separate traditional EOF analyses were performed on three-month subsets of the 250-hPa zonal wind anomaly data. These independent EOF analyses (not shown) confirm that EOF 1 and EOF 2 represent the two leading modes of NPJ variability with fidelity throughout the cool season.

The 250-hPa zonal wind anomalies at any particular analysis time can be regressed onto EOF 1 and EOF 2 to calculate the instantaneous principal components (PCs), PC 1 and PC 2, corresponding to that analysis time. The magnitude and sign of PC 1 and PC 2 are standardized and provide an indication of how strongly the instantaneous 250-hPa zonal wind anomalies project onto EOF 1 and EOF 2, respectively. Time series constructed from the instantaneous PCs subsequently assist in characterizing the temporal evolution of the NPJ with respect to EOF 1 and EOF 2. As noted by Griffin and Martin (2017), the use of instantaneous PCs produces a noisy time series due to the high-frequency variability that characterizes the NPJ on daily time scales (their Fig. 1). Consequently, in an attempt to describe the evolution of the NPJ with greater temporal coherence than the instantaneous PCs while preserving the high-frequency variability of the NPJ on daily time scales, the instantaneous PCs are smoothed through the calculation of a weighted average of the instantaneous PCs within ±24 h of each analysis time, t_0.

204 The weight, w, prescribed to the instantaneous PCs at each analysis time, t, within ±24 h of t_0 is
205 defined as: $w = 5 - |t - t_0|/6$, for $|t - t_0| \leq 24$ h.
206 The weighted PCs at a particular analysis time can then be plotted on a two-dimensional
207 Cartesian grid (i.e., the NPJ Phase Diagram) in an effort to visualize the state of the NPJ. The
208 position along the abscissa within the NPJ Phase Diagram corresponds to the value of weighted
209 PC 1 and indicates how strongly the 250-hPa zonal wind anomalies project onto EOF 1. Positive
210 and negative values of weighted PC 1 represent a jet extension and jet retraction, respectively.
211 The position along the ordinate within the NPJ Phase Diagram corresponds to the value of
212 weighted PC 2 and indicates how strongly the 250-hPa zonal wind anomalies project onto EOF
213 2. Positive and negative values of weighted PC 2 represent a poleward shift and equatorward
214 shift, respectively. Examples of NPJ configurations that project strongly onto a jet extension and
215 a jet retraction regime are provided in Figs. 2a and 2b, respectively, while NPJ configurations
216 that project strongly onto a poleward shift and an equatorward shift regime are provided in Figs.
217 3a and 3b, respectively.
218 As for the sample cases shown in Figs. 2 and 3, the weighted PCs at all analysis times
219 during 1979–2014 excluding the summer months are plotted on the NPJ Phase Diagram in order
220 to classify each analysis time into one of the four NPJ regimes, or to identify analysis times
221 during which the NPJ lies within the unit circle (Fig. 4). For this classification scheme, the
222 analysis times are classified based on, first, whether the position of the NPJ within the NPJ Phase
223 Diagram is greater than a distance of 1 PC unit from the origin and, second, whether the absolute
224 value of PC 1 or PC 2 is greater. Analysis times that fall into the "origin" category are
225 interpreted as times during which the NPJ exhibits a neutral signal with respect to the NPJ Phase
226 Diagram. Plotting the weighted PCs onto the NPJ Phase Diagram over a specified time interval

captures the evolution of the NPJ and yields a trajectory within the NPJ Phase Diagram.

3. Characteristics of the NPJ Phase Diagram

The classification of analysis times discussed in section 2 reveals several salient characteristics of each NPJ regime. The typical residence time of the NPJ within each NPJ regime is provided in Table 1. Overall, the mean and median residence time within an NPJ regime do not vary considerably between the NPJ regimes. Specifically, the mean residence time within an NPJ regime ranges between 3.58 and 3.85 days, while the median residence time ranges between 2.50 and 2.75 days. The residence time is slightly longer for periods when the NPJ resides within the unit circle, with a mean and median residence time of 4.65 and 3.25 days, respectively. The inequality between the mean and median residence times for each NPJ regime highlights the degree to which the distribution of residence times is skewed towards transient rather than persistent NPJ regimes. In support of this observation, an examination of the minimum and maximum residence time within each NPJ regime indicates that while an NPJ regime can be transient, it can also persist for multiple weeks.

As demonstrated from previous studies on NPJ variability, each NPJ regime exhibits a strong influence on the character of the downstream large-scale flow pattern over North America (e.g., Athanasiadis et al. 2010; Jaffe et al. 2011; Griffin and Martin 2017). To ensure consistency with previous studies, composite analyses are constructed employing the CFSR for periods during which the NPJ resided within the same NPJ regime for at least three consecutive days. A three-day threshold is chosen as a compromise between the magnitude of the mean and median residence time for each NPJ regime (Table 1). Figures 5 and 6 illustrate the characteristic large-scale flow pattern four days following the onset of each NPJ regime. This particular time is chosen to highlight both the characteristic structure of the NPJ as well as the downstream flow

pattern over North America associated with each NPJ regime. Two-sided Student's *t* tests were performed on the geopotential height and temperature anomaly fields shown in Figs. 5 and 6, respectively, to identify anomalies that are statistically significant with respect to climatology at the 99% confidence level.

A jet extension is characterized by the meridional juxtaposition of an anomalous upper-tropospheric trough over the central North Pacific and an anomalous ridge over the subtropical North Pacific that combine to produce a strong, zonally oriented NPJ (Fig. 5a). Beneath the left-exit region of the extended NPJ, an anomalous surface cyclone induces anomalous southerly geostrophic flow along the west coast of North America (Fig. 6a). This southerly geostrophic flow is collocated with lower-tropospheric warm anomalies over western North America as well as an anomalous upper-tropospheric ridge in the same location (Fig. 5a). Lower-tropospheric cold anomalies are found upstream of the surface cyclone in association with anomalous northerly geostrophic flow over the central North Pacific, and across eastern North America beneath an anomalous upper-tropospheric trough (Fig. 6a).

A jet retraction features an anomalous upper-tropospheric ridge over the central North Pacific, and anomalous troughs over northwestern North America and the subtropical North Pacific (Fig. 5b). In combination, these geopotential height anomalies result in a retracted NPJ over the western North Pacific and a split NPJ to the east of the dateline. Directly beneath the central North Pacific ridge, the circulation concomitant with an anomalous surface anticyclone is associated with lower-tropospheric cold anomalies over Alaska and the west coast of North America, and warm anomalies over the central North Pacific (Fig. 6b). Lower-tropospheric warm anomalies are also found in the south-central U.S. upstream of an anomalous upper-tropospheric ridge positioned over the southeastern U.S.

A poleward shift exhibits an anomalous upper-tropospheric trough over the high-latitude North Pacific and an anomalous ridge over the subtropical North Pacific that act in combination to position the exit region of the NPJ poleward of 40°N (Fig. 5c). An anomalous surface cyclone is located beneath the left-exit region of the poleward-shifted NPJ, which results in anomalous southerly geostrophic flow within an area characterized by lower-tropospheric warm anomalies over northern North America (Fig. 6c). These lower-tropospheric warm anomalies are also associated with an anomalous upper-tropospheric ridge positioned over eastern Canada (Fig. 5c). Lower-tropospheric cold anomalies are only observed over the Bering Strait and Gulf of Alaska during a poleward shift in conjunction with anomalous northerly geostrophic flow upstream of the surface cyclone (Fig. 6c).

Lastly, an equatorward shift is associated with an anomalous upper-tropospheric ridge over the high-latitude North Pacific and an anomalous trough over the subtropical North Pacific (Fig. 5d), reminiscent of a Rex block (Rex 1950). This configuration of geopotential height anomalies results in an equatorward deflection of the exit region of the NPJ near the dateline, and a weaker NPJ over the western North Pacific compared to the other NPJ regimes. An anomalous upper-tropospheric trough is also positioned over eastern Canada downstream of the high-latitude ridge over the North Pacific (Fig. 5d). In the lower-troposphere, an equatorward shift is associated with an anomalous surface anticyclone centered near the Aleutian Islands. This surface anticyclone induces anomalous northerly geostrophic flow within an area characterized by lower-tropospheric cold anomalies downstream of the surface anticyclone over northern North America (Fig. 6d). Conversely, anomalous southerly geostrophic flow upstream of the surface anticyclone is associated with the presence of lower-tropospheric warm anomalies over the Bering Strait and the Gulf of Alaska.

296 Consideration of the interannual and intraannual variability of each NPJ regime offers
297 insight into the characteristic structure of the NPJ. While the NPJ resides within one of the four
298 NPJ regimes (i.e., outside a radius of 1 PC unit from the origin) 59% of the time during an
299 average cool season (not shown), there is considerable interannual variability in the frequency of
300 each NPJ regime (Fig. 7a). As an example, the 1997–1998 cool season was characterized by the
301 second-lowest annual frequency of poleward shifts (4.7%), while the subsequent 1998–1999 cool
302 season featured the highest annual frequency of poleward shifts (34.9%). Comparable abrupt
303 changes in the annual frequency of an individual NPJ regime are readily observed when
304 considering the time series for other NPJ regimes. Furthermore, linear regressions performed on
305 each of the time series shown in Fig. 7a do not identify any statistically significant trends in the
306 frequency of each NPJ regime during 1979–2014 (not shown).
307 There is considerable intraannual variability in the frequency of each NPJ regime, as well
308 (Fig. 7b). Specifically, the NPJ resides within an NPJ regime most frequently during November–
309 March and less frequently during the months of September, October, April, and May. Both jet
310 extensions and jet retractions peak in frequency during the month of March, while poleward
311 shifts and equatorward shifts peak during February and January, respectively. The frequencies of
312 each NPJ regime during an individual month are generally comparable, except during March,
313 when jet extensions and jet retractions are noticeably more frequent than poleward shifts and
314 equatorward shifts, and during September, when poleward shifts and equatorward shifts are
315 considerably more frequent than jet extensions and jet retractions.
316 As might be anticipated, the interannual and intraannual frequency of each NPJ regime
317 are strongly modulated by large-scale atmospheric teleconnection patterns. For example, the
318 Pacific–North American (PNA) pattern is known to be strongly related to the intensity of the

NPJ (e.g., Wallace and Gutzler 1981; Barnston and Livesey 1987; Franzke and Feldstein 2005; Strong and Davis 2008; Athanasiadis et al. 2010; Franzke et al. 2011; Griffin and Martin 2017). Specifically, a positive PNA pattern is characterized by an anomalous upper-tropospheric trough over the central North Pacific and an anomalous ridge over the subtropical North Pacific. Consequently, a positive PNA pattern is conducive to an extended (Fig. 5a) or poleward-shifted NPJ (Fig. 5c). Conversely, a negative PNA pattern exhibits an anomalous upper-tropospheric ridge over the central North Pacific, which favors a retracted (Fig. 5b) or equatorward-shifted NPJ (Fig. 5d).

To illustrate the relationship between the PNA and each NPJ regime, all analysis times that were characterized by an NPJ regime (i.e., outside a radius of 1 PC unit from the origin) were classified based on the sign and magnitude of the daily PNA index (CPC 2017a). Analysis times that featured a PNA index > 0.5 were classified as occurring during a positive PNA, those that featured a PNA index < –0.5 were classified as occurring during a negative PNA, and those remaining were classified as occurring during a neutral PNA. Figure 8a demonstrates that the frequency of each NPJ regime is well associated with the phase of the PNA. In particular, a positive PNA is most frequently characterized by jet extensions and poleward shifts, while a negative PNA is most frequently characterized by jet retractions and equatorward shifts.

The frequency of each NPJ regime also exhibits an association with the phase of the Arctic Oscillation (AO; Thompson and Wallace 1998; Higgins et al. 2000; Ambaum et al. 2001). The positive (negative) phase of the AO is characterized by above-normal (below-normal) 1000-hPa geopotential heights over the central North Pacific and below-normal (above-normal) 1000-hPa geopotential heights over the Arctic. As for the PNA index, daily AO indices (CPC 2017b) are employed to classify analysis times that were characterized by an NPJ regime. Analysis times

342 exhibiting an AO index > 0.5 were classified as occurring during a positive AO, those exhibiting
343 an AO index < –0.5 were classified as occurring during a negative AO, and those remaining were
344 classified as occurring during a neutral AO. Figure 8b indicates that a positive AO is most
345 frequently characterized by jet retractions and a negative AO is most frequently characterized by
346 jet extensions. This relationship agrees with the NPJ regime composites shown in Figs. 6b and
347 6a, given that jet retractions are associated with an anomalous surface anticyclone over the
348 central North Pacific (Fig. 6b), and jet extensions feature an anomalous surface cyclone in that
349 location (Fig. 6a).

350 The El Niño–Southern Oscillation (ENSO) also modulates the structure of the NPJ. For
351 example, prior work suggests that anomalous convection and above-normal sea surface
352 temperatures over the central and eastern equatorial Pacific during an El Niño favor an extended
353 or equatorward-shifted NPJ. Conversely, anomalous convection and above-normal sea-surface
354 temperatures over the western equatorial Pacific during a La Niña favor a retracted or poleward-
355 shifted NPJ (e.g., Horel and Wallace 1981; Rasmusson and Wallace 1983; Rasmusson and Mo
356 1993; Yang et al. 2002; Xie et al. 2015; Cook et al. 2017). In an effort to frame this relationship
357 with respect to the NPJ Phase Diagram, analysis times that were characterized by an NPJ regime
358 were classified based on the sign and magnitude of the monthly Niño-3.4 index (ESRL 2017).
359 Analysis times that coincided with a Niño-3.4 index > 1.0 were classified as occurring during an
360 El Niño, those that coincided with a Niño-3.4 index < –1.0 were classified as occurring during a
361 La Niña, and those remaining were classified as occurring during a neutral ENSO state. Figure
362 8c demonstrates that El Niño is most frequently characterized by jet extensions and equatorward
363 shifts. Conversely, La Niña is most frequently characterized by jet retractions and poleward
364 shifts. The results from Fig. 8c translate to individual cool seasons characterized by El Niño and

La Niña events, as well. For example, Fig. 7a indicates that the 1982–1983 El Niño cool season (Sep–May Niño 3.4 = 1.82) was most frequently characterized by jet extensions and equatorward shifts, while the 1999–2000 La Niña cool season (Sep–May Niño 3.4 = –1.22) was most frequently characterized by jet retractions and poleward shifts.

4. GEFS forecast skill with respect to the NPJ Phase Diagram

Given the relationship between each NPJ regime and the downstream large-scale flow pattern over North America (Figs. 5 and 6), additional knowledge of the forecast skill associated with each NPJ regime offers the potential to increase confidence in operational medium-range forecasts over North America. To evaluate the forecast skill associated with each NPJ regime, an ensemble of 9-day forecast trajectories within the NPJ Phase Diagram are calculated daily during 1985–2014 excluding the summer months using 250-hPa zonal wind data from the 1.0°-resolution GEFS Reforecast Version 2 dataset (Hamill et al. 2013). The GEFS Reforecast dataset features 10 ensemble member forecasts and 1 control member forecast initialized daily at 0000 UTC, each with forecast lead times as long as 384 h.

Forecast errors within the NPJ Phase Diagram are calculated as the distance error in PC units between the ensemble mean NPJ Phase Diagram forecast and the verifying 0-h analysis that corresponds to each forecast lead time. The NPJ Phase Diagram forecasts are then classified based on (1) the position of the NPJ within the NPJ Phase Diagram at the time of forecast initialization or forecast verification according to the schematic shown in Fig. 4 and (2) season. Two-sided Student's *t* tests are performed on all NPJ Phase Diagram forecast error statistics to assess statistical significance in accordance with the specifications described in each pertinent figure caption.

The average distance errors associated with ensemble mean NPJ Phase Diagram forecasts

initialized during the same season are provided in Fig. 9a. At lead times ≤ 120 h, NPJ Phase Diagram forecasts initialized during the winter (Dec–Feb) exhibit significantly larger distance errors within the NPJ Phase Diagram than forecasts initialized during the fall (Sep–Nov) and spring (Mar–May). At lead times ≥ 168 h, forecasts initialized during the winter and spring exhibit significantly larger distance errors than forecasts initialized during the fall. Furthermore, forecasts initialized during the fall exhibit distance errors that fall below the cool-season average at all forecast lead times, while forecasts initialized during the winter exhibit errors that lie above the cool-season average at all forecast lead times.

The average distance errors of ensemble mean NPJ Phase Diagram forecasts initialized during the same NPJ regime are shown in Fig. 9b. At lead times < 120 h, no significant differences in distance error are observed between the NPJ regimes. However, significant differences between the NPJ regimes begin to emerge at lead times ≥ 120 h. Specifically, forecasts initialized during a jet retraction exhibit significantly larger distance errors than forecasts initialized during a poleward shift at lead times between 120 h and 168 h, and significantly larger distance errors than forecasts initialized during a jet extension at lead times between 192 h and 216 h. However, despite these significant differences at lead times ≥ 120 h, the spread in distance errors between the NPJ regimes is generally small during this time period.

The average distance errors of ensemble mean NPJ Phase Diagram forecasts verified during the same NPJ regime are shown in Fig. 9c. At lead times ≥ 144 h, forecasts verified during equatorward shifts and jet retractions exhibit significantly larger distance errors than those verified during poleward shifts and jet extensions. Additionally, considerably larger spread between the distance errors associated with each NPJ regime is observed for NPJ Phase Diagram forecasts verified during the same NPJ regime (Fig. 9c) compared to those initialized during the

411 same NPJ regime (Fig. 9b) for this time period. Consequently, knowledge of the NPJ regime at
412 the time of forecast verification appears to be a greater indicator of forecast skill with respect to
413 the NPJ Phase Diagram than the NPJ regime at the time of forecast initialization. This result
414 implies that enhanced or reduced confidence can be ascribed to a forecast by considering the
415 forecast evolution of the NPJ with respect to the NPJ Phase Diagram, rather than by considering
416 the state of the NPJ at the time of forecast initialization.

417 The poor forecast skill of ensemble mean NPJ Phase Diagram forecasts verified during
418 equatorward shifts (Fig. 9c) is also apparent when considering the frequency with which each
419 NPJ regime is overforecast or underforecast in the GEFS Reforecast dataset. Figure 10
420 demonstrates that equatorward shifts are substantially underforecast by ensemble mean NPJ
421 Phase Diagram forecasts at all lead times compared to the verifying 0-h analyses. Specifically,
422 equatorward shifts are underforecast by nearly 26% at a 216-h lead time, which is at least twice
423 the frequency that the other NPJ regimes are underforecast at the same lead time. While all NPJ
424 regimes are generally underforecast by the ensemble mean NPJ Phase Diagram forecasts at lead
425 times $\geq$ 192 h, both jet extensions and poleward shifts are overforecast at lead times $\leq$ 144 h.

426 **5. Best and worst NPJ Phase Diagram forecasts**

427 An examination of the best and worst NPJ Phase Diagram medium-range forecasts has
428 the potential to illuminate factors that may contribute to enhanced or reduced forecast skill
429 during the medium-range period (e.g., Lillo and Parsons 2017). The best and worst medium-
430 range forecasts with respect to the NPJ Phase Diagram are identified as those forecasts that rank
431 in the top or bottom 10%, respectively, in terms of both (1) the GEFS ensemble mean distance
432 error averaged over the 192-h and 216-h forecasts and (2) the GEFS ensemble member distance
433 error averaged over all ensemble members for the 192-h and 216-h forecasts. The first criterion

provides a measure of forecast accuracy during the medium-range period, while the second criterion provides a measure of forecast precision.

Figure 11 describes a series of hypothetical NPJ Phase Diagram forecasts that would qualify as a best, an intermediate, and a worst forecast with respect to the two criteria identified in the previous paragraph. A best forecast is one in which the forecast exhibits a small average ensemble mean distance error and a small average ensemble member distance error. Therefore, a best forecast is interpreted as one in which the forecast is both accurate and precise. An intermediate forecast is one in which there is a small average ensemble mean distance error but also a large average ensemble member distance error. Consequently, both criteria are not satisfied and this situation represents one in which the forecast was accurate but not precise. Finally, a worst forecast is one in which there is a large average ensemble mean distance error and a large average ensemble member distance error. Such a forecast is characteristic of one that is neither accurate nor precise.

The frequency distribution of the worst NPJ Phase Diagram forecasts during the cool season features two separate maxima during December and March and two separate minima during September and January (Fig. 12a). The best NPJ Phase Diagram forecasts occur most frequently at the beginning and end of the cool season during September and May, respectively, but also during December. The best and worst NPJ Phase Diagram forecasts are classified based on the NPJ regime at the time of forecast initialization in Fig. 12b. This frequency distribution indicates that the worst forecasts are initialized disproportionately more than the best forecasts during jet retractions and equatorward shifts, while the best forecasts are initialized disproportionately more than the worst forecasts during jet extensions and poleward shifts. The average value of PC 1 and PC 2 at the time of forecast initialization (Table 2) also indicates a

457 preference for the worst forecasts to be initialized most frequently during jet retractions and
458 equatorward shifts, and for the best forecasts to be initialized most frequently during jet
459 extensions and poleward shifts. However, only the values of PC 1 are significantly different
460 between the best and worst forecasts at the time of forecast initialization.

461 The evolution of the NPJ during the 10-day period following the initialization of a best
462 and worst NPJ Phase Diagram forecast also differs considerably (Table 2). In particular, the
463 average change in PC 2 (ΔPC 2) during the 10-day period following the initialization of a worst
464 forecast indicates a significant movement of the NPJ towards an equatorward shift within the
465 NPJ Phase Diagram, while the ΔPC 2 following the initialization of a best forecast indicates a
466 significant movement of the NPJ towards a poleward shift. Additionally, the worst forecast
467 periods feature significantly longer trajectories within the NPJ Phase Diagram compared to the
468 best forecast periods during the 10-day period following forecast initialization (Table 2). As will
469 be demonstrated, this result is consistent with the notion that the worst forecasts often occur
470 during periods characterized by rapid NPJ regime change, while the best forecast periods are
471 often characterized by more persistent upper-tropospheric flow patterns over the North Pacific in
472 comparison. This notion aligns well with previous work suggesting that periods characterized by
473 upper-tropospheric regime change are generally associated with reduced forecast skill (e.g.,
474 Tibaldi and Molteni 1990; Frederiksen et al. 2004; Pelly and Hoskins 2006; Ferranti et al. 2015;
475 Lillo and Parsons 2017).

476 An examination of the upper-tropospheric flow patterns associated with the best and
477 worst forecast periods offers insight into the types of large-scale flow patterns that are
478 characterized by enhanced or reduced forecast skill. This examination is performed by
479 employing the CFSR to construct composite analyses of 250-hPa wind speed, geopotential

480 height, and geopotential height anomalies at the time a best and worst forecast are initialized, as
481 well as at 192 h following forecast initialization. Two-sided Student's *t* tests are used to evaluate
482 whether the differences between geopotential height anomalies associated with the worst and
483 best forecast composites are statistically significant at the 99% confidence level at each time
484 period.

485 The composite upper-tropospheric flow patterns at the time a best and worst forecast are
486 initialized within each NPJ regime are provided in Fig. 13. At first glance, an examination of the
487 geopotential height anomalies in Fig. 13 reveals minor qualitative differences between the best
488 and worst forecasts that are initialized during the same NPJ regime. However, a calculation of
489 the difference between geopotential height anomalies associated with the worst and best
490 forecasts reveals some significant features (Fig. 14). In particular, while both the best and worst
491 forecasts that are initialized during a jet extension exhibit a strong, zonally extended NPJ at the
492 time of forecast initialization (Figs. 13a,b), the worst forecasts are characterized by significantly
493 higher geopotential height anomalies over the eastern North Pacific compared to the best
494 forecasts (Fig. 14a). Similarly, while both the best and worst forecasts that are initialized during
495 a jet retraction feature an anomalous ridge over the central North Pacific (Figs. 13c,d), the worst
496 forecasts also exhibit significantly higher geopotential height anomalies over the eastern North
497 Pacific compared to the best forecasts (Fig. 14b). The worst forecasts that are initialized during a
498 jet retraction also feature significantly lower geopotential height anomalies over the subtropical
499 North Pacific and the western Great Lakes compared to the best forecasts (Fig. 14b).

500 Similar to jet extensions and jet retractions, the worst forecasts that are initialized during
501 a poleward shift exhibit significantly higher geopotential height anomalies over the eastern North
502 Pacific compared to the best forecasts (Figs. 13e,f and 14c). Furthermore, the worst forecasts that

503 are initialized during a poleward shift feature a more intense NPJ, a stronger jet stream over
504 North America, and significantly lower geopotential height anomalies over the southwestern
505 U.S. and northwestern Mexico compared to the best forecasts (Figs. 13e,f and 14c). While not as
506 large in magnitude compared to the other composites, the worst forecasts that are initialized
507 during an equatorward shift also exhibit significantly higher geopotential height anomalies over
508 the eastern North Pacific compared to the best forecasts (Figs. 13g,h and 14d). Consequently, the
509 presence of higher geopotential height anomalies over the eastern North Pacific at the time of
510 forecast initialization is a distinguishing factor between the worst and best forecasts regardless of
511 the prevailing NPJ regime.

512 Substantial differences in the upper-tropospheric flow pattern over the North Pacific are
513 observed 192 h following the initialization of a best and worst forecast. In particular, the upper-
514 tropospheric flow pattern 192 h following the initialization of a best forecast is characterized by
515 the meridional juxtaposition of an anomalous trough and an anomalous ridge over the central
516 North Pacific regardless of the NPJ regime at the time of forecast initialization (Figs. 15a,c,e,g).
517 This pattern subsequently favors an NPJ that is extended and poleward-shifted in the best
518 forecast composites relative to the worst forecast composites. Downstream of the anomalous
519 trough over the North Pacific, an anomalous ridge is also firmly positioned over North America
520 in the best forecast composites. In contrast to the best forecasts, the upper-tropospheric flow
521 pattern 192 h following the initialization of a worst forecast features an anomalous ridge over the
522 high-latitude North Pacific and a retracted NPJ regardless of the NPJ regime at the time of
523 forecast initialization (Figs. 15b,d,f,h). An anomalous trough of variable strength is also located
524 over North America in all of the worst forecast composites.

525 The difference between the geopotential height anomalies 192 h following the

initialization of a worst and best forecast is shown in Fig. 16. Compared to the best forecast composites, all of worst forecast composites exhibit significantly higher geopotential height anomalies over the high-latitude North Pacific, and significantly lower geopotential height anomalies over the subtropical North Pacific (Figs. 16a–d), reminiscent of a Rex block (Rex 1950). Notably, this difference pattern prevails regardless of the NPJ regime at the time of forecast initialization. Consequently, the upper-tropospheric flow patterns shown in Fig. 16 uniformly suggest that periods characterized by the development and/or maintenance of upper-tropospheric blocking events over the North Pacific are associated with reduced forecast skill with respect to the NPJ Phase Diagram. Conversely, reversing the sign of the difference field in Fig. 16 (not shown) suggests that periods evolving towards a zonal NPJ over the North Pacific are generally associated with enhanced forecast skill.

6. Discussion and conclusions

The preceding analysis corroborates the results from prior studies on NPJ variability that establish a relationship between the two leading modes of 250-hPa zonal wind variability over the North Pacific and the large-scale flow pattern over North America (e.g., Athanasiadis et al. 2010; Jaffe et al. 2011; Griffin and Martin 2017). Provided with this relationship, this study utilizes the two leading modes of 250-hPa zonal wind variability from the CFSR during the cool season as the foundation for developing an NPJ Phase Diagram. The NPJ Phase Diagram subsequently provides an objective tool to monitor the state and evolution of the upper-tropospheric flow pattern over the North Pacific, to identify the prevailing NPJ regime, and to evaluate the characteristic forecast skill associated with each NPJ regime.

The application of the NPJ Phase Diagram to 250-hPa zonal wind data from the CFSR during 1979–2014 excluding the summer months reveals several salient characteristics of each

549 NPJ regime and highlights opportunities for additional research. For example, while the mean
550 and median residence times within a particular NPJ regime are typically on the order of three
551 days, an NPJ regime can persist for multiple weeks. Furthermore, it is apparent that the
552 frequency of each NPJ regime is characterized by considerable interannual and intraannual
553 variability. Given that each NPJ regime can strongly influence the character of the downstream
554 flow pattern over North America, further investigation into the types of large-scale flow patterns
555 that are conducive to prolonged residence times within an NPJ regime, or that increase the
556 frequency of an NPJ regime, may add considerable value to operational seasonal and subseasonal
557 forecasts over North America.

558 Large-scale atmospheric teleconnection patterns, such as the PNA, AO, and ENSO, are
559 one such factor that can strongly modulate the frequency of each NPJ regime. For example, it
560 was noted that a positive (negative) PNA is most frequently characterized by jet extensions and
561 poleward shifts (jet retractions and equatorward shifts). Jet extensions and poleward shifts are
562 associated with different lower-tropospheric temperature anomaly patterns over North America,
563 however, with jet extensions favoring anomalously cold temperatures over eastern North
564 America and poleward shifts favoring anomalously warm temperatures over northern North
565 America. Consequently, knowledge of the prevailing NPJ regime in combination with the phase
566 of the PNA index provides additional value to operational forecasts of temperature over North
567 America. The NPJ Phase Diagram provides an objective basis for detailed investigations of NPJ
568 variability during other well-established atmospheric teleconnection patterns, as well, such as the
569 North Atlantic Oscillation (e.g., Wallace and Gutzler 1981) and Madden–Julian Oscillation
570 (Madden and Julian 1972). Such investigations have the potential to identify the variety of large-
571 scale flow evolutions over the North Pacific that occur during a particular atmospheric

572 teleconnection pattern.

573 An examination of the forecast skill associated with each NPJ regime reveals the types of
574 large-scale flow patterns that exhibit reduced forecast skill with respect to the NPJ Phase
575 Diagram. In particular, the analysis suggests that forecasts verified during jet retractions and
576 equatorward shifts exhibit significantly reduced forecast skill compared to jet extensions and
577 poleward shifts at lead times ≥ 144 h. Recall that both jet retractions and equatorward shifts are
578 typically characterized by an anomalous upper-tropospheric ridge in the central North Pacific. In
579 light of these two observations, and given that diabatic processes can play an important role in
580 amplifying the upper-tropospheric flow pattern (e.g., Massacand et al. 2001; Riemer et al. 2008;
581 Torn 2010; Ferranti et al. 2015; Pfahl et al. 2015; Grams and Archambault 2016; Bosart et al.
582 2017), it is hypothesized that diabatic processes account for a considerable fraction of the
583 reduced forecast skill associated with jet retractions and equatorward shifts. Additional case
584 study work that utilizes the NPJ Phase Diagram to investigate poor forecasts verified during jet
585 retractions and equatorward shifts is likely to determine the degree to which diabatic processes
586 contribute to the reduced forecast skill associated with these NPJ regimes.

587 An analysis of the best and worst medium-range forecasts with respect to the NPJ Phase
588 Diagram suggests that the worst forecasts are often associated with the development and/or
589 maintenance of upper-tropospheric blocking events over the North Pacific. This result aligns
590 well with previous work highlighting the reduced predictability associated with the development
591 and/or maintenance of blocking events (e.g., Tibaldi and Molteni 1990; D'Andrea et al. 1998;
592 Frederiksen et al. 2004; Pelly and Hoskins 2006; Matsueda 2011; Ferranti et al. 2015) and holds
593 regardless of the prevailing NPJ regime at the time of forecast initialization. Given this
594 variability in the prevailing NPJ regime prior to blocking events, additional work is required to

595 determine the types of large-scale flow evolutions that are most conducive to block development.
596 The NPJ Phase Diagram is well suited for such work by providing an objective frame of
597 reference from which to examine the spectrum of large-scale flow evolutions that are conducive
598 to block development. The analysis also indicates that the worst forecast periods are associated
599 with a significant movement of the NPJ towards an equatorward shift within the NPJ Phase
600 Diagram during the 10-day period following forecast initialization, while the best forecast
601 periods are associated with a significant movement of the NPJ towards a poleward shift. Given
602 that certain trajectories within the NPJ Phase Diagram are associated with reduced forecast skill,
603 the NPJ Phase Diagram represents a tool that can be used to objectively identify NPJ regime
604 transitions and to isolate the characteristic large-scale flow patterns associated with those regime
605 transitions. The results from such an investigation have the potential to add considerable value to
606 operational forecasts during periods of regime transition.
607 The relative forecast skill associated with each NPJ regime is only applicable with
608 respect to the GEFS Reforecast dataset in the present study. Consequently, additional research is
609 required to evaluate the forecast skill of NPJ regimes with respect to other ensemble prediction
610 systems (EPSs). An evaluation of forecast skill with respect to other EPSs has the potential to
611 determine whether the large-scale flow patterns that exhibit reduced skill in the GEFS Reforecast
612 dataset differ from those that exhibit reduced skill in other EPSs. To the degree that differences
613 exist in the forecast skill of each NPJ regime across EPSs, such an evaluation has the potential to
614 identify situations during which greater confidence can be ascribed to a particular EPS.
615
616 *Acknowledgments*
617 The authors thank Mike Bodner, Daniel Halperin, Arlene Laing, Bill Lamberson, Sara Ganetis,

618 and Josh Kastman for their constructive discussions concerning the NPJ Phase Diagram. The
619 authors also thank the National Oceanic and Atmospheric Administration for its support of this
620 work via Grant NA15NWS4680006 and the National Science Foundation for its support of this
621 work via Grant AGS-1355960.

622 REFERENCES

623 Ambaum, M. H. P., B. J. Hoskins, and D. B. Stephenson, 2001: Arctic Oscillation or North
624 Atlantic Oscillation? *J. Climate*, **14**, 3495–3507, doi: 10.1175/1520-
625 0442(2001)014<3495:AOONAO>2.0.CO;2.
626 Archambault, H. M., L. F. Bosart, D. Keyser, and J. M. Cordeira, 2013: A climatological
627 analysis of the extratropical flow response to recurving western North Pacific tropical
628 cyclones. *Mon. Wea. Rev.*, **141**, 2325–2346, doi: 10.1175/MWR-D-12-00257.1.
629 Archambault, H. M., D. Keyser, L. F. Bosart, C. A. Davis, and J. M. Cordeira, 2015: A
630 composite perspective of the extratropical flow response to recurving western North
631 Pacific tropical cyclones. *Mon. Wea. Rev.*, **143**, 1122–1141, doi: 10.1175/MWR-D-14-
632 00270.1.
633 Athanasiadis, P. J., J. M. Wallace, and J. J. Wettstein, 2010: Patterns of wintertime jet stream
634 variability and their relation to the storm tracks. *J. Atmos. Sci.*, **67**, 1361–1381, doi:
635 10.1175/2009JAS3270.1.
636 Barnston, A. G., and R. E. Livezey, 1987: Classification, seasonality and persistence of low-
637 frequency atmospheric circulation patterns. *Mon. Wea. Rev.*, **115**, 1083–1126, doi:
638 10.1175/1520-0493(1987)115<1083:CSAPOL>2.0.CO;2.
639 Bosart, L. F., B. J. Moore, J. M. Cordeira, and H. M. Archambault, 2017: Interactions of North
640 Pacific tropical, midlatitude, and polar disturbances resulting in linked extreme weather
641 events over North America in October 2007. *Mon. Wea. Rev.*, **145**, 1245–1273, doi:
642 10.1175/MWR-D-16-0230.1.
643 Chang, E. K. M., S. Lee, and K. L. Swanson, 2002: Storm track dynamics. *J. Climate*, **15**, 2163–
644 2183, doi: 10.1175/1520-0442(2002)015<02163:STD>2.0.CO;2.

Cook, A. R., L. M. Leslie, D. B. Parsons, and J. T. Schaefer, 2017: The impact of El Niño–Southern Oscillation (ENSO) on winter and early spring U.S. tornado outbreaks. *J. Appl. Meteor. Climatol.*, **56**, 2455–2478, doi: 10.1175/JAMC-D-16-0249.1.

CPC, 2017a: Pacific/North American pattern. Accessed 9 February 2017, http://www.cpc.ncep.noaa.gov/products/precip/CWlink/pna/pna.shtml.

CPC, 2017b: Arctic Oscillation. Accessed 9 February 2017, http://www.cpc.ncep.noaa.gov/products/precip/CWlink/daily_ao_index/ao.shtml.

D'Andrea, F., and Coauthors, 1998: Northern Hemisphere atmospheric blocking as simulated by 15 atmospheric general circulation models in the period 1979–1988. *Climate Dyn.*, **14**, 385–407, doi: 10.1007/s003820050230.

Eichelberger, S. J., and D. L. Hartmann, 2007: Zonal jet structure and the leading mode of variability. *J. Climate*, **20**, 5149–5163, doi: 10.1175/JCLI4279.1.

ESRL, 2017: Niño 3.4 SST Index. Accessed 5 January 2017, https://www.esrl.noaa.gov/psd/gcos_wgsp/Timeseries/Nino34/.

Ferranti, L., S. Corti, and M. Janousek, 2015: Flow-dependent verification of the ECMWF ensemble over the Euro-Atlantic sector. *Quart. J. Roy. Meteor. Soc.*, **141**, 916–924, doi: 10.1002/qj.2411.

Franzke, C., and S. B. Feldstein, 2005: The continuum and dynamics of Northern Hemisphere teleconnection patterns. *J. Atmos. Sci.*, **62**, 3250–3267, doi: 10.1175/JAS3536.1.

Franzke, C., S. B. Feldstein, and S. Lee, 2011: Synoptic analysis of the Pacific–North American teleconnection pattern. *Quart. J. Roy. Meteor. Soc.*, **137**, 329–346, doi: https://doi.org/10.1002/qj.768.

667 Frederiksen, J. S., M. A. Collier, and A. B. Watkins, 2004: Ensemble prediction of blocking
668 regime transitions. *Tellus*, **56A**, 485–500, doi: 10.1111/j.1600-0870.2004.00075.x.
669 Grams, C. M., and H. M. Archambault, 2016: The key role of diabatic outflow in amplifying the
670 midlatitude flow: A representative case study of weather systems surrounding western
671 North Pacific extratropical transition. *Mon. Wea. Rev.*, **144**, 3847–3869, doi:
672 10.1175/MWR-D-15-0419.1.
673 Griffin, K. S., and J. E. Martin, 2017: Synoptic features associated with temporally coherent
674 modes of variability of the North Pacific jet stream. *J. Climate*, **30**, 39–54, doi:
675 10.1175/JCLI-D-15-0833.1.
676 Hakim, G. J., 2003: Developing wave packets in the North Pacific storm track. *Mon. Wea. Rev.*,
677 **131**, 2824–2837, doi: 10.1175/1520-0493(2003)131<2824:DWPITN>2.0.CO;2.
678 Harr, P. A., and J. M. Dea, 2009: Downstream development associated with the extratropical
679 transition of tropical cyclones over the western North Pacific. *Mon. Wea. Rev.*, **137**,
680 1295–1319, doi: 10.1175/2008MWR2558.1.
681 Hamill, T. M., G. T. Bates, J. S. Whitaker, D. R. Murray, M. Fiorino, T. J. Galarneau Jr., Y. Zhu,
682 and W. Lapenta, 2013: NOAA's second-generation global medium-range ensemble
683 reforecast dataset. *Bull. Amer. Meteor. Soc.*, **94**, 1553–1565, doi: 10.1175/BAMS-D-12-
684 00014.1.
685 Handlos, Z. J., and J. E. Martin, 2016: Composite analysis of large-scale environments
686 conducive to western Pacific polar/subtropical jet superposition. *J. Climate*, **29**, 7145–
687 7165, doi: 10.1175/JCLI-D-16-0044.1.

688 Higgins, R. W., J.-K. E. Schemm, W. Shi, and A. Leetmaa, 2000: Extreme precipitation events
689 in the western United States related to tropical forcing. *J. Climate*, **13**, 793–820, doi:
690 10.1175/1520-0442(2000)013<0793:EPEITW>2.0.CO;2.
691 Horel, J. D., and J. M. Wallace, 1981: Planetary-scale atmospheric phenomena associated with
692 the Southern Oscillation. *Mon. Wea. Rev.*, **109**, 813–829, doi: 10.1175/1520-
693 0493(1981)109<0813:PSAPAW>2.0.CO;2.
694 Hoskins, B. J., and D. J. Karoly, 1981: The steady linear response of a spherical atmosphere to
695 thermal and orographic forcing. *J. Atmos. Sci.*, **38**, 1179–1196, doi: 10.1175/1520-
696 0469(1981)038<1179:TSLROA>2.0.CO;2.
697 Jaffe, S. C., J. E. Martin, D. J. Vimont, and D. J. Lorenz, 2011: A synoptic climatology of
698 episodic, subseasonal retractions of the Pacific jet. *J. Climate*, **24**, 2846–2860, doi:
699 10.1175/2010JCLI3995.1.
700 Jhun, J.-G., and E.-J. Lee, 2004: A new East Asian winter monsoon index and associated
701 characteristics of the winter monsoon. *J. Climate*, **17**, 711–726, doi: 10.1175/1520-
702 0442(2004)017<0711:ANEAWM>2.0.CO;2.
703 Kalnay, E., and Coauthors, 1996: The NCEP/NCAR 40-year reanalysis project. *Bull. Amer.*
704 *Meteor. Soc.*, **77**, 437–471, doi: 10.1175/1520-0477(1996)077<0437:TNYRP>2.0.CO;2.
705 Lee, Y.-Y., G.-H. Lim, and J.-S. Kug, 2010: Influence of the East Asian winter monsoon on the
706 storm track activity over the North Pacific. *J. Geophys. Res.*, **115**, D09102, doi:
707 10.1029/2009JD012813.
708 Lillo, S. P., and D. B. Parsons, 2017: Investigating the dynamics of error growth in ECMWF
709 medium-range forecast busts. *Quart. J. Roy. Meteor. Soc.*, **143**, 1211–1226, doi:
710 10.1002/qj.2938.

711 Lin, H., and J. Derome, 1996: Changes in predictability associated with the PNA pattern. *Tellus*,
712 **48A**, 553–571, doi: 10.1034/j.1600-0870.1996.t01-3-00005.x.
713 Madden, R. A., and P. R. Julian, 1972: Description of global-scale circulation cells in the tropics
714 with a 40–50 day period. *J. Atmos. Sci.*, **29**, 1109–1123, doi: 10.1175/1520-
715 0469(1972)029<1109:DOGSCC>2.0.CO;2.
716 Madden, R. A., and P. R. Julian, 1994: Observations of the 40–50-day tropical oscillation—A
717 review. *Mon. Wea. Rev.*, **122**, 814–837, doi: 10.1175/1520-
718 0493(1994)122<0814:OOTDTO>2.0.CO;2.
719 Massacand, A. C., H. Wernli, and H. C. Davies, 2001: Influence of upstream diabatic heating
720 upon an alpine event of heavy precipitation. *Mon. Wea. Rev.*, **129**, 2822–2828, doi:
721 10.1175/1520-0493(2001)129<2822:IOUDHU>2.0.CO;2.
722 Matsueda, M., 2011: Predictability of Euro-Russian blocking in summer of 2010. *Geophys. Res.*
723 *Lett.*, **38**, L06801, doi: 10.1029/2010GL046557.
724 North, G. R., T. L. Bell, R. F. Cahalan, and F. J. Moeng, 1982: Sampling errors in the estimation
725 of empirical orthogonal functions. *Mon. Wea. Rev.*, **110**, 699–706, doi: 10.1175/1520-
726 0493(1982)110<0699:SEITEO>2.0.CO;2.
727 Orlanski, I., and J. P. Sheldon, 1995: Stages in the energetics of baroclinic systems. *Tellus*, **47A**,
728 605–628, doi: 10.1034/j.1600-0870.1995.00108.x.
729 Palmer, T. N., 1988: Medium and extended range predictability and stability of the Pacific/North
730 American mode. *Quart. J. Roy. Meteor. Soc.*, **114**, 691–713. doi:
731 10.1002/qj.49711448108.
732 Pelly J. L., and B. J. Hoskins, 2006: How well does the ECMWF Ensemble Prediction System
733 predict blocking? *Quart. J. Roy. Meteor. Soc*., **129**, 1683–1702, doi: 10.1256/qj.01.173.

734 Pfahl, S., C. Schwierz, M. Croci-Maspoli, C. M. Grams, and H. Wernli, 2015: Importance of
735 latent heat release in ascending air streams for atmospheric blocking. *Nat. Geosci.*, **8**,
736 610–614, doi: 10.1038/ngeo2487.
737 Rasmusson, E. M., and J. M. Wallace, 1983: Meteorological aspects of the El Niño/Southern
738 Oscillation. *Science*, **222**, 1195–1202, doi: 10.1126/science.222.4629.1195.
739 Rasmusson, E. M., and K. Mo, 1993: Linkages between 200-mb tropical and extratropical
740 circulation anomalies during the 1986–1989 ENSO cycle. *J. Climate*, **6**, 595–616, doi:
741 10.1175/1520-0442(1993)006<0595:LBMTAE>2.0.CO;2.
742 Rex, D. F., 1950: Blocking action in the middle troposphere and its effect upon regional climate.
743 I: An aerological study of blocking action. *Tellus*, **2A**, 196–211, doi: 10.1111/j.2153-
744 3490.1950.tb00331.x.
745 Riemer, M., S. C. Jones, and C. A. Davis, 2008: The impact of extratropical transition on the
746 downstream flow: An idealized modelling study with a straight jet. *Quart. J. Roy.*
747 *Meteor. Soc.*, **134**, 69–91, doi: 10.1002/qj.189.
748 Saha, S., and Coauthors, 2010: The NCEP Climate Forecast System Reanalysis. *Bull. Amer.*
749 *Meteor. Soc.*, **91**, 1015–1057, doi: 10.1175/2010BAMS3001.1.
750 Saha, S., and Coauthors, 2014: The NCEP Climate Forecast System version 2. *J. Climate*, **27**,
751 2185–2208, doi: 10.1175/JCLI-D-12-00823.1.
752 Schubert, S. D., and C.-K. Park, 1991: Low-frequency intraseasonal tropical–extratropical
753 interactions. *J. Atmos. Sci.*, **48**, 629–650, doi: 10.1175/1520-
754 0469(1991)048<0629:LFITEI>2.0.CO;2.

755 Sheng, J., 2002: GCM experiments on changes in atmospheric predictability associated with the
756 PNA pattern and tropical SST anomalies. *Tellus*, **54A**, 317–329, doi: 10.1034/j.1600-
757 0870.2002.01324.x.
758 Strong, C., and R. E. Davis, 2008: Variability in the position and strength of winter jet stream
759 cores related to Northern Hemisphere teleconnections. *J. Climate*, **21**, 584–592, doi:
760 10.1175/2007JCLI1723.1.
761 Tibaldi, S., and F. Molteni, 1990: On the operational predictability of blocking. *Tellus*, **42A**,
762 343–365, doi: 10.1034/j.1600-0870.1990.t01-2-00003.x.
763 Thompson, D. W. J., and J. M. Wallace, 1998: The Arctic oscillation signature in wintertime
764 geopotential height and temperature fields. *Geophys. Res. Lett.*, **25**, 1297–1300, doi:
765 10.1029/98GL00950.
766 Torn, R. D., 2010: Diagnosis of the downstream ridging associated with extratropical transition
767 using short-term ensemble forecasts. *J. Atmos. Sci.*, **67**, 817–833, doi:
768 10.1175/2009JAS3093.1.
769 Torn, R. D., and G. J. Hakim, 2015: Comparison of wave packets associated with extratropical
770 transition and winter cyclones. *Mon. Wea. Rev.*, **143**, 1782–1803, doi: 10.1175/MWR-D-
771 14-00006.1.
772 Wallace, J. M., and D. S. Gutzler, 1981: Teleconnections in the geopotential height field during
773 the Northern Hemisphere winter. *Mon. Wea. Rev.*, **109**, 784–812, doi: 10.1175/1520-
774 0493(1981)109<0784:TITGHF>2.0.CO;2.
775 Wang, L., and W. Chen, 2014: An intensity index for the East Asian winter monsoon. *J. Climate*,
776 **27**, 2361–2374, doi: 10.1175/JCLI-D-13-00086.1.

777 Weare, B. C., and J. S. Nasstrom, 1982: Examples of extended empirical orthogonal function
778 analyses. *Mon. Wea. Rev.*, **110**, 481–485, doi:10.1175/1520-0493(1982)110,0481:
779 EOEEOF.2.0.CO;2.
780 Wilks, D. S., 2011: Statistical Methods in the Atmospheric Sciences. 3rd ed. Elsevier, 676 pp.
781 Xie, Z., Y. Du, and S. Yang, 2015: Zonal extension and retraction of the subtropical westerly jet
782 stream and evolution of precipitation over East Asia and the western Pacific. *J. Climate*,
783 **28**, 6783–6798, doi: 10.1175/JCLI-D-14-00649.1.
784 Yang, S., K.-M. Lau, and K.-M. Kim, 2002: Variations of the East Asian jet stream and Asian–
785 Pacific–American winter climate anomalies. *J. Climate*, **15**, 306–325, doi: 10.1175/1520-
786 0442(2002)015<0306:VOTEAJ>2.0.CO;2.
787

Table Captions

TABLE 1. Characteristic residence times in days for each NPJ regime. The numbers in parentheses represent the number of analysis times characterized by each NPJ regime during 1979–2014 excluding the summer months (Jun–Aug).

TABLE 2. NPJ Phase Diagram characteristics derived from the CFSR for the periods characterized by the best and worst NPJ Phase Diagram medium-range forecasts with all quantities expressed in PC units. ΔPC 1 and ΔPC 2 represent the change in PC 1 and PC 2, respectively, during the 10-day period following the initialization of a best and worst forecast. Asterisks indicate that values associated with the best and worst forecasts are statistically significantly different at the 99.9% confidence level.

811 **Tables**

General NPJ Regime Characteristics				
NPJ Regime	Mean Residence Time (d)	Median Residence Time (d)	Maximum Residence Time (d)	Minimum Residence Time (d)
Jet Extension (N=5842)	3.85	2.50	27.25	0.25
Jet Retraction (N=5685)	3.70	2.75	34.00	0.25
Poleward Shift (N=6164)	3.58	2.75	18.00	0.25
Equatorward Shift (N=5437)	3.65	2.50	18.50	0.25
Origin (N=16212)	4.65	3.25	35.50	0.25

812

813 TABLE 1. Characteristic residence times in days for each NPJ regime. The numbers in
814 parentheses represent the number of analysis times characterized by each NPJ regime during
815 1979–2014 excluding the summer months (Jun–Aug).
816
817

818

819

820

821

822

823

824

Comparison of Best/Worst Forecast Periods					
	Avg. Start PC 1	Avg. Start PC 2	Avg. ΔPC 1	Avg. ΔPC 2	Avg. 10-d Traj. Length
Best Forecasts (N=475)	0.09*	0.04	0.09	0.16*	3.50*
Worst Forecasts (N=763)	−0.18*	−0.08	0.01	−0.21*	4.33*

TABLE 2. NPJ Phase Diagram characteristics derived from the CFSR for the periods characterized by the best and worst NPJ Phase Diagram medium-range forecasts with all quantities expressed in PC units. ΔPC 1 and ΔPC 2 represent the change in PC 1 and PC 2, respectively, during the 10-day period following the initialization of a best and worst forecast. Asterisks indicate that values associated with the best and worst forecasts are statistically significantly different at the 99.9% confidence level.

848 **Figure Captions**

849 FIG. 1. (a) September–May 250-hPa mean zonal wind is contoured in black every 10 m s^{-1}
850 above 30 m s^{-1}, and the regression of EOF 1 onto 250-hPa zonal wind anomaly data is shaded
851 following the legend in m s^{-1}. (b) As in (a) but for EOF 2.

852

853 FIG. 2. (a) 250-hPa wind speed in m s^{-1} is shaded following the legend at 1800 UTC 11 February
854 2004. (b) The location of weighted PC 1 and PC 2 at 1800 UTC 11 February 2004 within the
855 NPJ Phase Diagram. (c),(d) As in (a),(b) but for 1800 UTC 13 March 2009.

856

857 FIG. 3. As in Fig. 2, but for (a),(b) 1800 UTC 9 April 1984 and (c),(d) 1200 UTC 28 January
858 1991.

859

860 FIG. 4. Schematic illustrating the classification scheme for CFSR analysis times and GEFS
861 reforecasts with respect to the NPJ Phase Diagram.

862

863 FIG. 5. Composite mean 250-hPa wind speed in m s^{-1} is shaded in the fill pattern, 250-hPa
864 geopotential height is contoured in black every 120 m, and 250-hPa geopotential height
865 anomalies are contoured in solid red and dashed blue every 30 m for positive and negative
866 values, respectively, 4 days following the initiation of a (a) jet extension, (b) jet retraction, (c)
867 poleward shift, and (d) equatorward shift regime. The number in the bottom right of each panel
868 indicates the number of cases included in each composite. Stippled areas represent locations
869 where the 250-hPa geopotential height anomalies are statistically significantly different from
870 climatology at the 99% confidence level.

871

872 FIG. 6. Composite anomalies of mean sea-level pressure are contoured in solid and dashed black
873 every 2 hPa for positive and negative values, respectively, and 850-hPa temperature anomalies
874 are shaded in the fill pattern every 1 K 4 days following the initiation of a (a) jet extension, (b)
875 jet retraction, (c) poleward shift, and (d) equatorward shift regime. The number in the bottom
876 right of each panel indicates the number of cases included in each composite. Stippled areas
877 represent locations where the 850-hPa temperature anomalies are statistically significantly
878 different from climatology at the 99% confidence level.

879

880 FIG. 7. (a) The percent frequency of analysis times during every cool season between September
881 1979 and May 2014 that are characterized by each NPJ regime. The years indicated on the
882 horizontal axis identify the end of individual cool seasons. (b) The percent frequency of analysis
883 times during each month of the cool season that are characterized by each NPJ regime. The
884 numbers in parentheses below each month indicate the number of analysis times during each
885 month.

886

887 FIG. 8. (a) The percent frequency of each NPJ regime at analysis times during which the NPJ is
888 outside of the unit circle on the NPJ Phase Diagram and characterized by each phase of the PNA
889 discussed in the text. The numbers in parentheses below each category indicate the number of
890 analysis times in each category. (b) As in (a), but for the AO. (c) As in (a), but for ENSO.

891

892 FIG. 9. (a) The average error of GEFS ensemble mean NPJ Phase Diagram forecasts initialized
893 during the same season. The colored circles on each line indicate that the error associated with

894 that season is statistically significantly different from the error associated with another season at
895 the 99% confidence level. The numbers in parentheses in the legend indicate the number of
896 forecasts in that category. Forecast lead time on the horizontal axis represents the hours after
897 forecast initialization. (b) As in (a), but for forecasts initialized during the same NPJ regime. (c)
898 As in (a), but for forecasts verified during the same NPJ regime. Forecast lead time on the
899 horizontal axis in (c) depicts the hours prior to forecast verification.
900
901 FIG. 10. The percent frequency that an NPJ regime is overforecast or underforecast by the GEFS
902 ensemble mean NPJ Phase Diagram forecasts relative to the verifying 0-h analyses at each
903 forecast lead time.
904
905 FIG. 11. Schematic illustrating the classification scheme for the best and worst NPJ Phase
906 Diagram medium-range forecasts.
907
908 FIG. 12. (a) The percent frequency of the best and worst NPJ Phase Diagram medium-range
909 forecasts that are initialized during each month of the cool season. (b) The percent frequency of
910 the best and worst NPJ Phase Diagram medium-range forecasts that are initialized during each
911 NPJ regime.
912
913 FIG. 13. Composite mean 250-hPa wind speed in m s^{-1} is shaded in the fill pattern, 250-hPa
914 geopotential height is contoured in black every 120 m, and 250-hPa geopotential height
915 anomalies are contoured in solid red and dashed blue every 30 m for positive and negative
916 values, respectively, at the time a (a) best and (b) worst NPJ Phase Diagram forecast are

initialized during a jet extension. (c),(d) As in (a),(b), but for those forecasts that are initialized during a jet retraction. (e),(f) As in (a),(b), but for those forecasts that are initialized during a poleward shift. (g),(h) As in (a),(b), but for those forecasts that are initialized during an equatorward shift. The quantities in the top right corner of every panel indicate the number of cases included in each composite.

FIG. 14. (a) The difference between the 250-hPa geopotential height anomalies associated with a worst and best NPJ Phase Diagram forecast at the time of forecast initialization during a jet extension is shaded every 30 m in the fill pattern. (b) As in (a), but during a jet retraction. (c) As in (a), but during a poleward shift. (d) As in (a), but during an equatorward shift. Statistically significant differences in geopotential height anomalies at the 99% confidence level are stippled in all panels.

FIG. 15. As in Fig. 13, but for the composite 250-hPa flow patterns 192 h following the initialization of a best and worst NPJ Phase Diagram forecast.

FIG. 16. As in Fig. 14, but for the composite difference between 250-hPa geopotential height anomalies 192 h following the initialization of a worst and best NPJ Phase Diagram forecast.

945 **Figures**

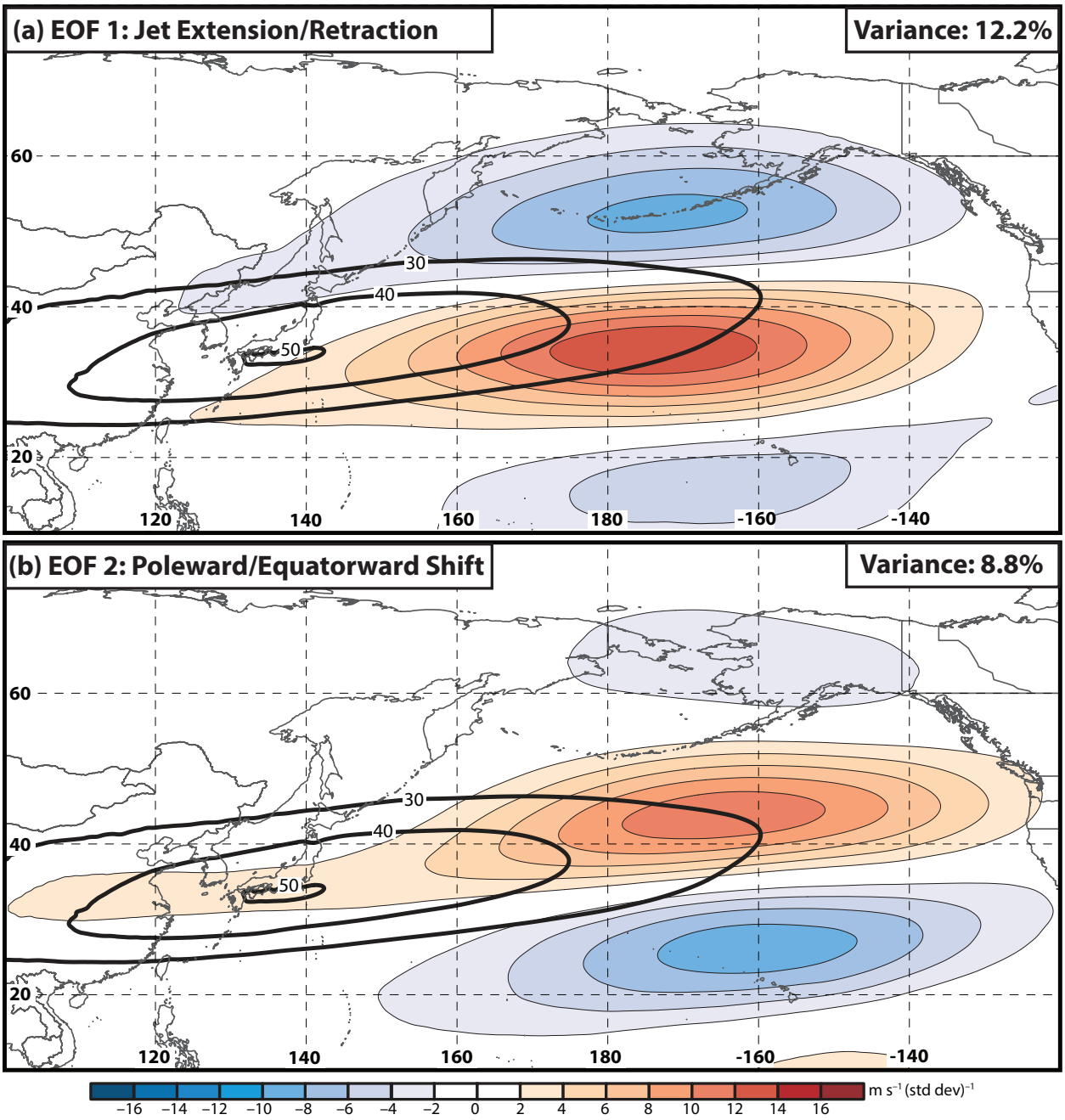

946
947
948 FIG. 1. (a) September–May 250-hPa mean zonal wind is contoured in black every 10 m s^{-1}
949 above 30 m s^{-1}, and the regression of EOF 1 onto 250-hPa zonal wind anomaly data is shaded
950 following the legend in m s^{-1}. (b) As in (a) but for EOF 2.
951

952

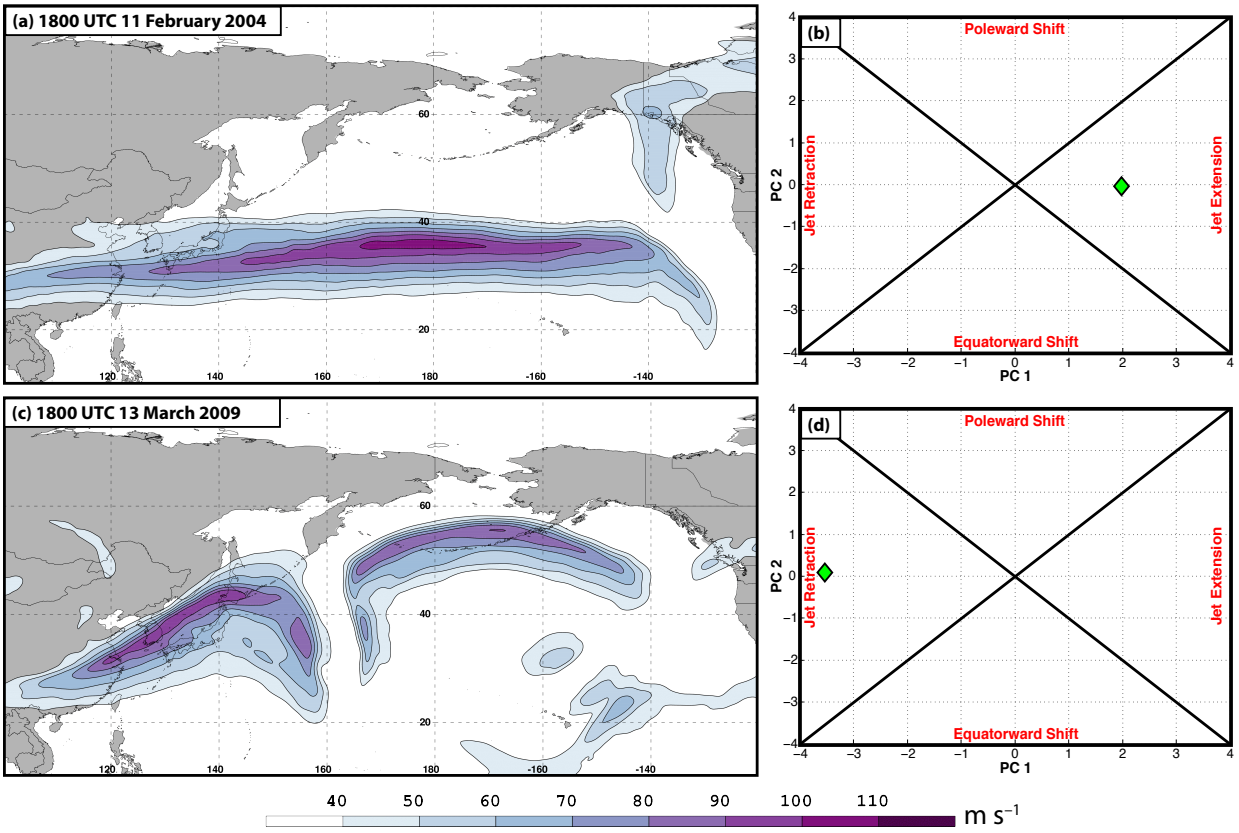

FIG. 2. (a) 250-hPa wind speed in m s^{-1} is shaded following the legend at 1800 UTC 11 February 2004. (b) The location of weighted PC 1 and PC 2 at 1800 UTC 11 February 2004 within the NPJ Phase Diagram. (c),(d) As in (a),(b) but for 1800 UTC 13 March 2009.

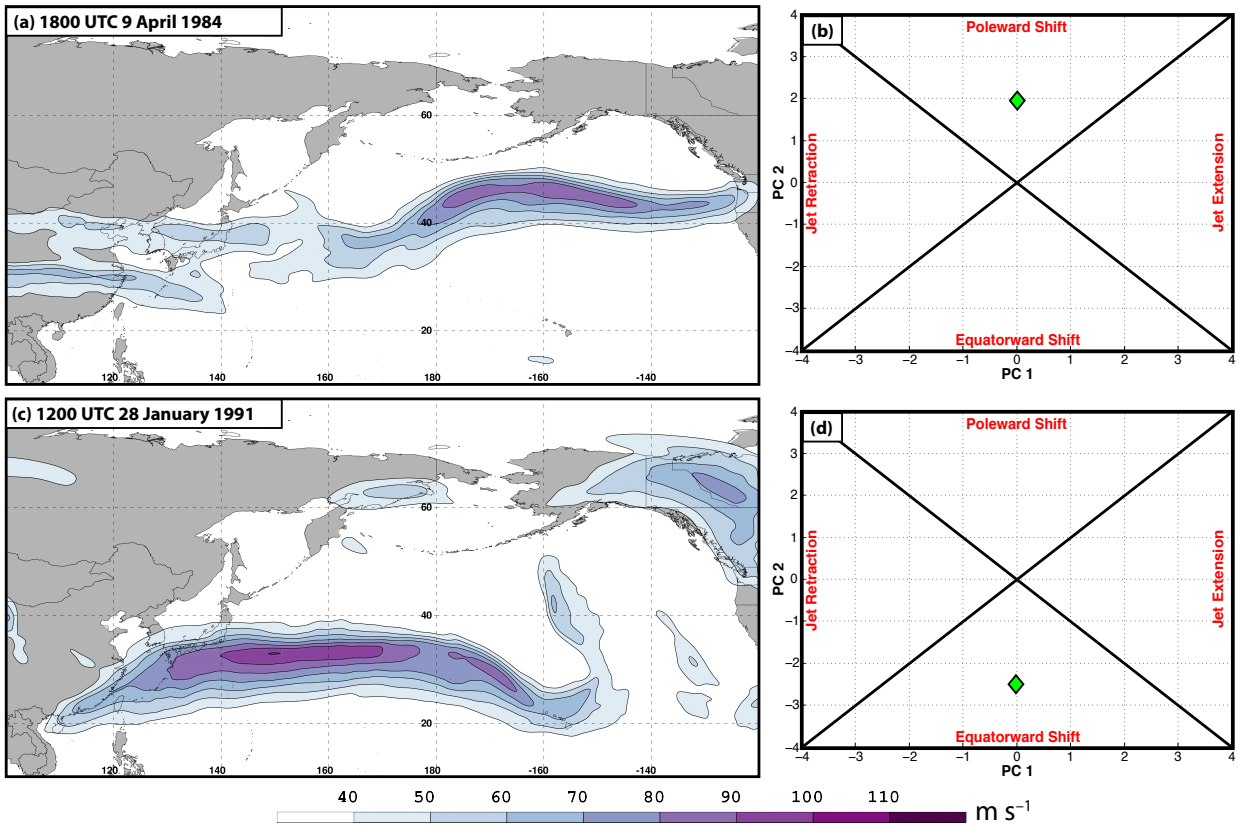

FIG. 3. As in Fig. 2, but for (a),(b) 1800 UTC 9 April 1984 and (c),(d) 1200 UTC 28 January 1991.

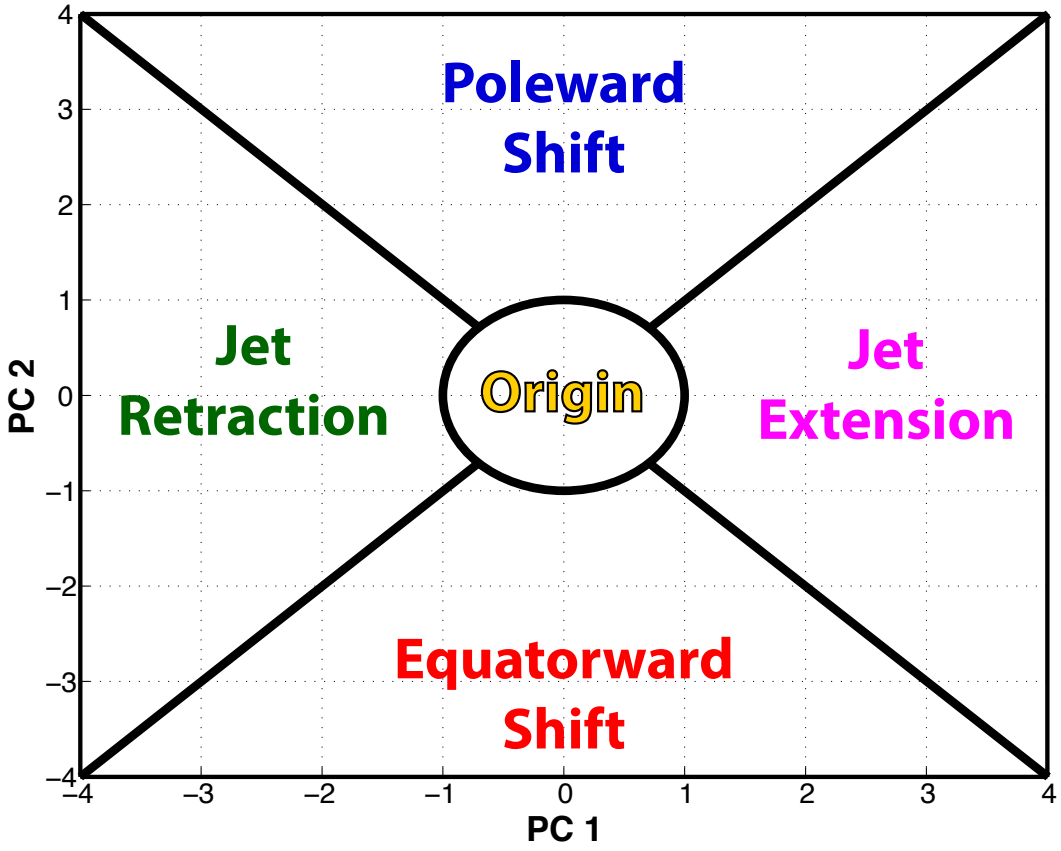

FIG. 4. Schematic illustrating the classification scheme for CFSR analysis times and GEFS reforecasts with respect to the NPJ Phase Diagram.

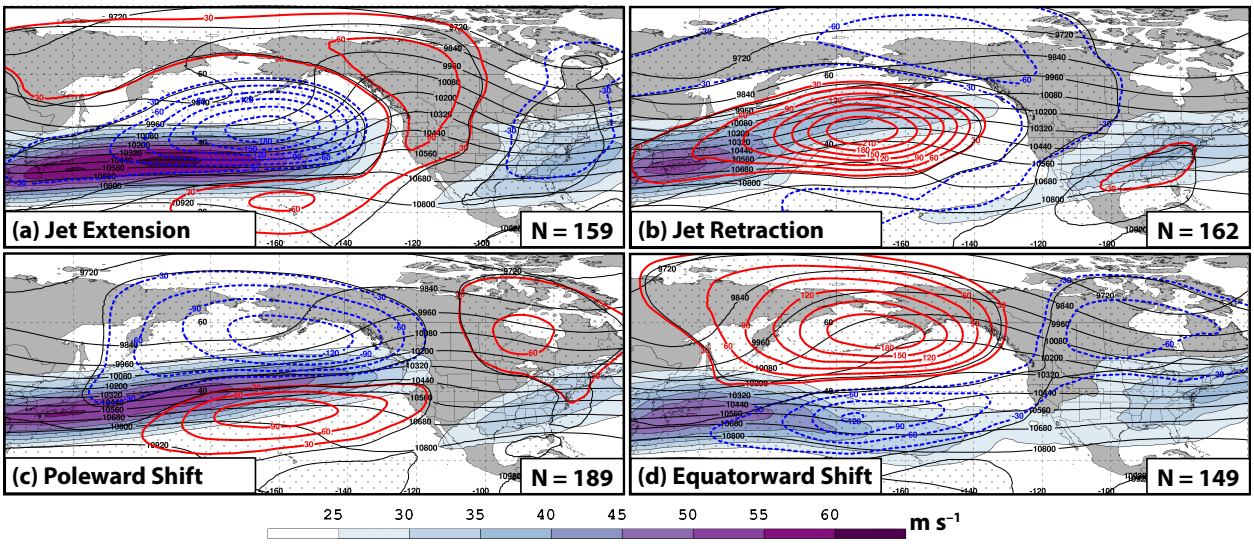

FIG. 5. Composite mean 250-hPa wind speed in m s^{-1} is shaded in the fill pattern, 250-hPa geopotential height is contoured in black every 120 m, and 250-hPa geopotential height anomalies are contoured in solid red and dashed blue every 30 m for positive and negative values, respectively, 4 days following the initiation of a (a) jet extension, (b) jet retraction, (c) poleward shift, and (d) equatorward shift regime. The number in the bottom right of each panel indicates the number of cases included in each composite. Stippled areas represent locations where the 250-hPa geopotential height anomalies are statistically significantly different from climatology at the 99% confidence level.

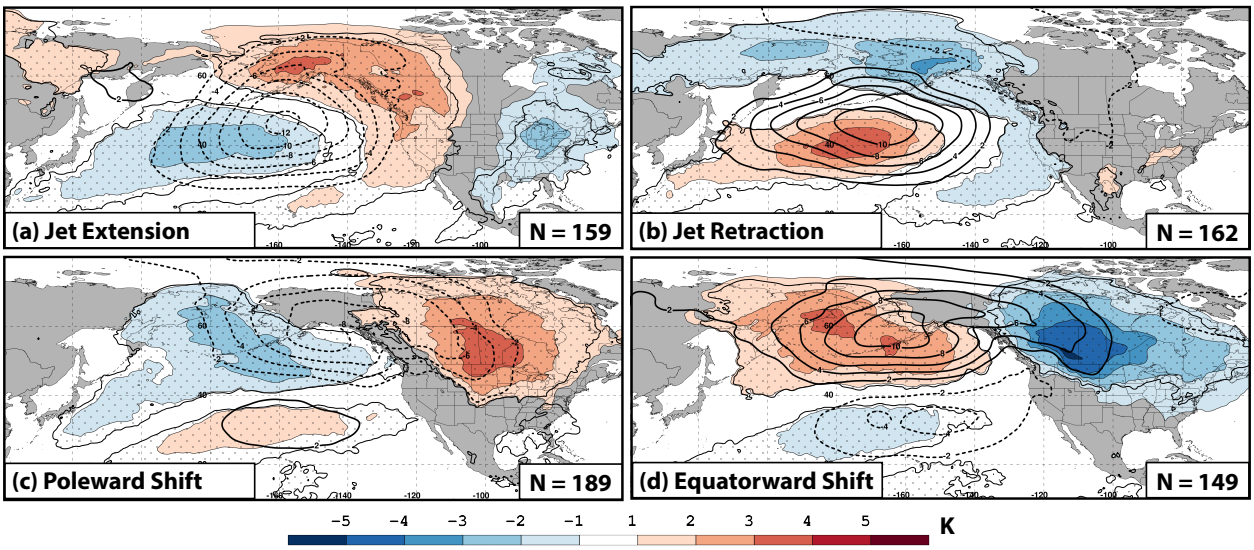

FIG. 6. Composite anomalies of mean sea-level pressure are contoured in solid and dashed black every 2 hPa for positive and negative values, respectively, and 850-hPa temperature anomalies are shaded in the fill pattern every 1 K 4 days following the initiation of a (a) jet extension, (b) jet retraction, (c) poleward shift, and (d) equatorward shift regime. The number in the bottom right of each panel indicates the number of cases included in each composite. Stippled areas represent locations where the 850-hPa temperature anomalies are statistically significantly different from climatology at the 99% confidence level.

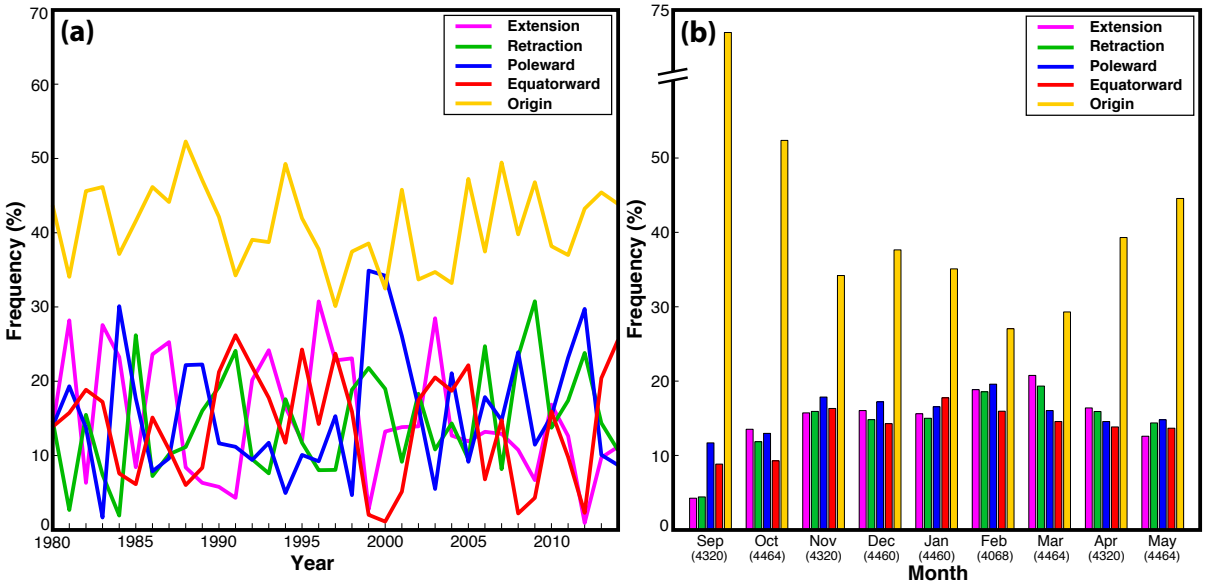

FIG. 7. (a) The percent frequency of analysis times during every cool season between September 1979 and May 2014 that are characterized by each NPJ regime. The years indicated on the horizontal axis identify the end of individual cool seasons. (b) The percent frequency of analysis times during each month of the cool season that are characterized by each NPJ regime. The numbers in parentheses below each month indicate the number of analysis times during each month.

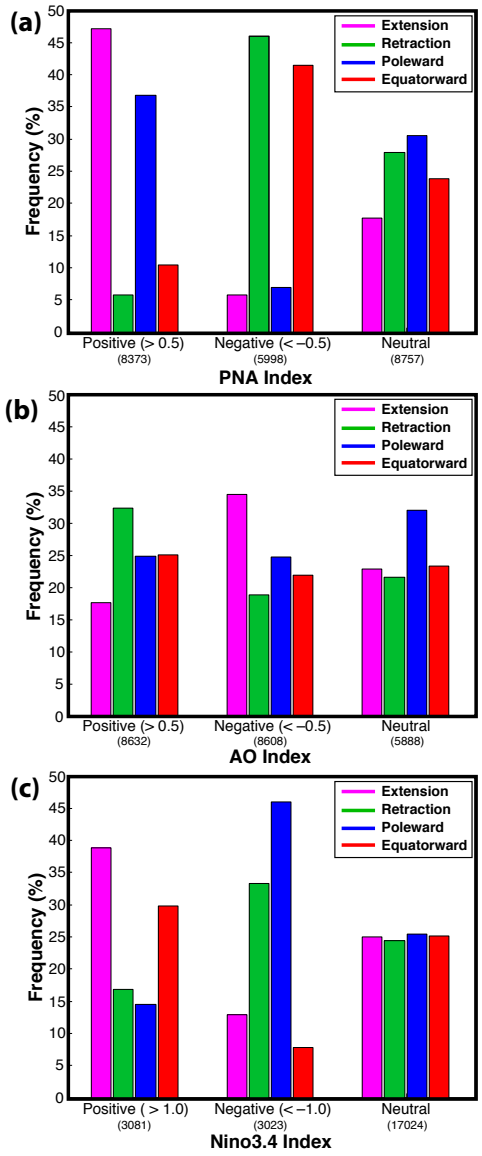

FIG. 8. (a) The percent frequency of each NPJ regime at analysis times during which the NPJ is outside of the unit circle on the NPJ Phase Diagram and characterized by each phase of the PNA discussed in the text. The numbers in parentheses below each category indicate the number of analysis times in each category. (b) As in (a), but for the AO. (c) As in (a), but for ENSO.

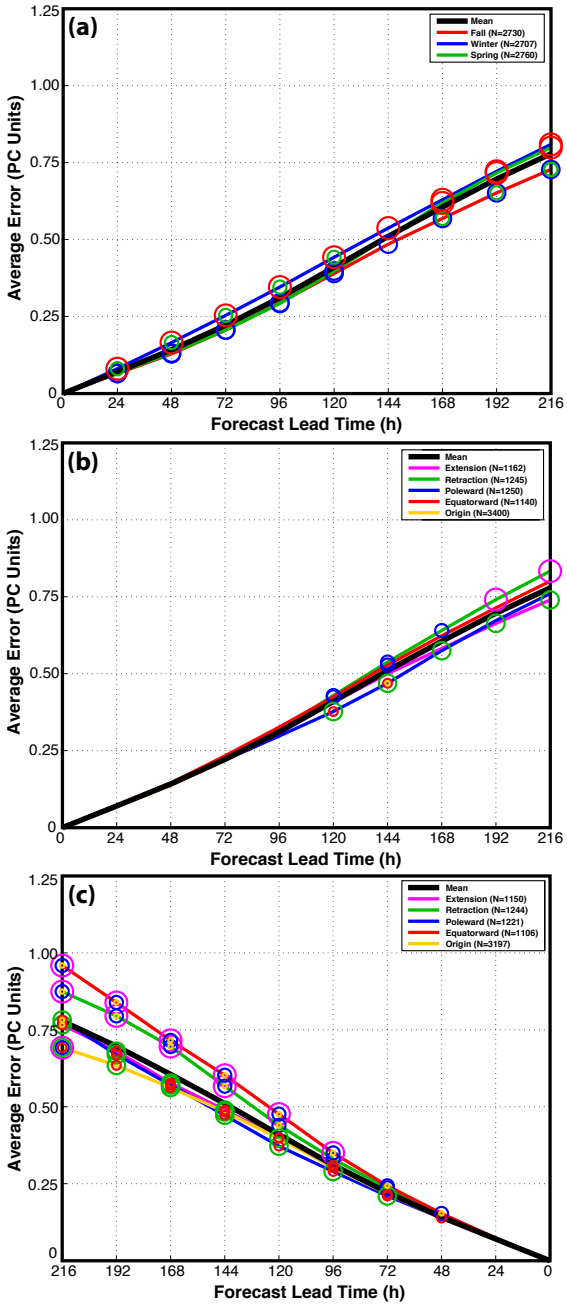

FIG. 9. (a) The average error of GEFS ensemble mean NPJ Phase Diagram forecasts initialized during the same season. The colored circles on each line indicate that the error associated with that season is statistically significantly different from the error associated with another season at the 99% confidence level. The numbers in parentheses in the legend indicate the number of forecasts in that category. Forecast lead time on the horizontal axis represents the hours after forecast initialization. (b) As in (a), but for forecasts initialized during the same NPJ regime. (c) As in (a), but for forecasts verified during the same NPJ regime. Forecast lead time on the horizontal axis in (c) depicts the hours prior to forecast verification.

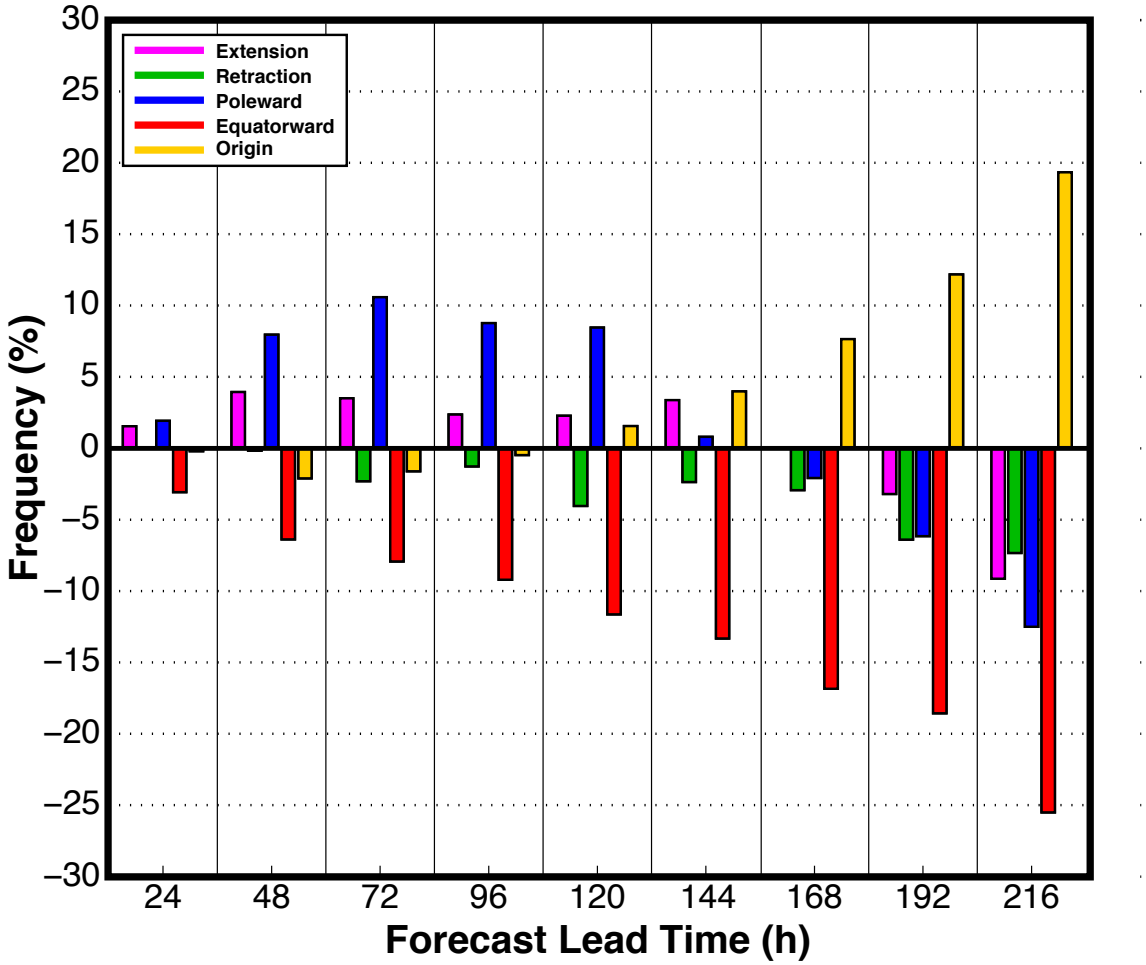

1141
1142 FIG. 10. The percent frequency that an NPJ regime is overforecast or underforecast by the GEFS
1143 ensemble mean NPJ Phase Diagram forecasts relative to the verifying 0-h analyses at each
1144 forecast lead time.
1145

1146

1147

1148

1149

1150

1151

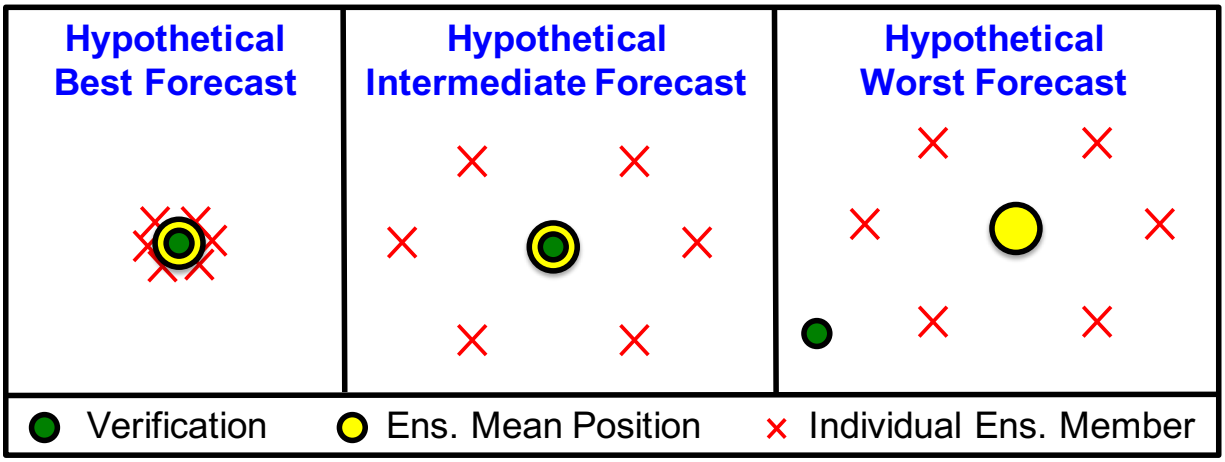

FIG. 11. Schematic illustrating the classification scheme for the best and worst NPJ Phase Diagram medium-range forecasts.

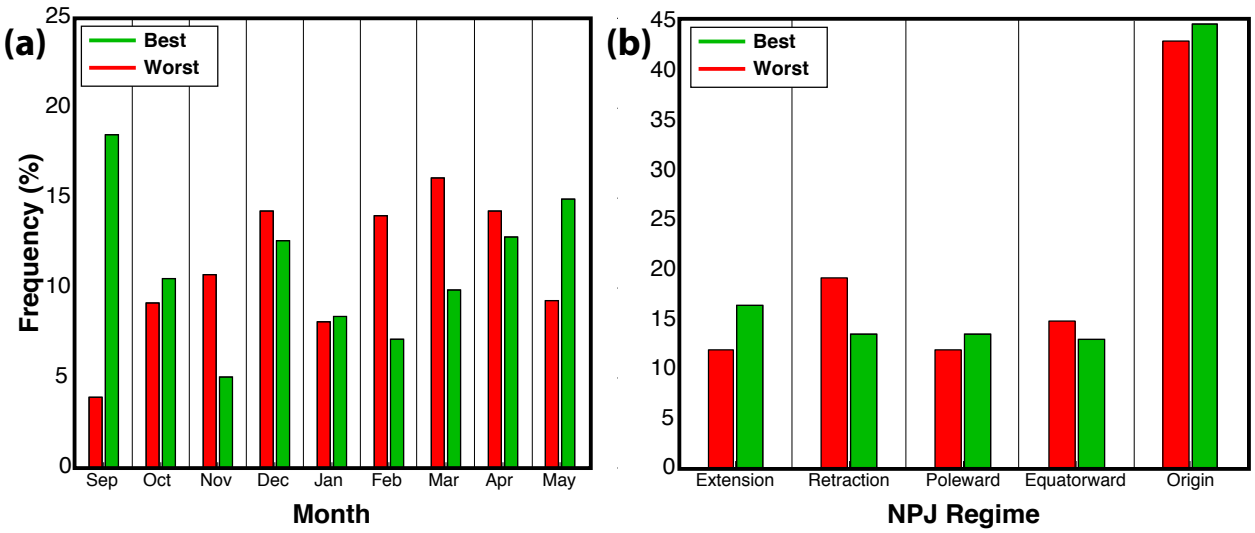

FIG. 12. (a) The percent frequency of the best and worst NPJ Phase Diagram medium-range forecasts that are initialized during each month of the cool season. (b) The percent frequency of the best and worst NPJ Phase Diagram medium-range forecasts that are initialized during each NPJ regime.

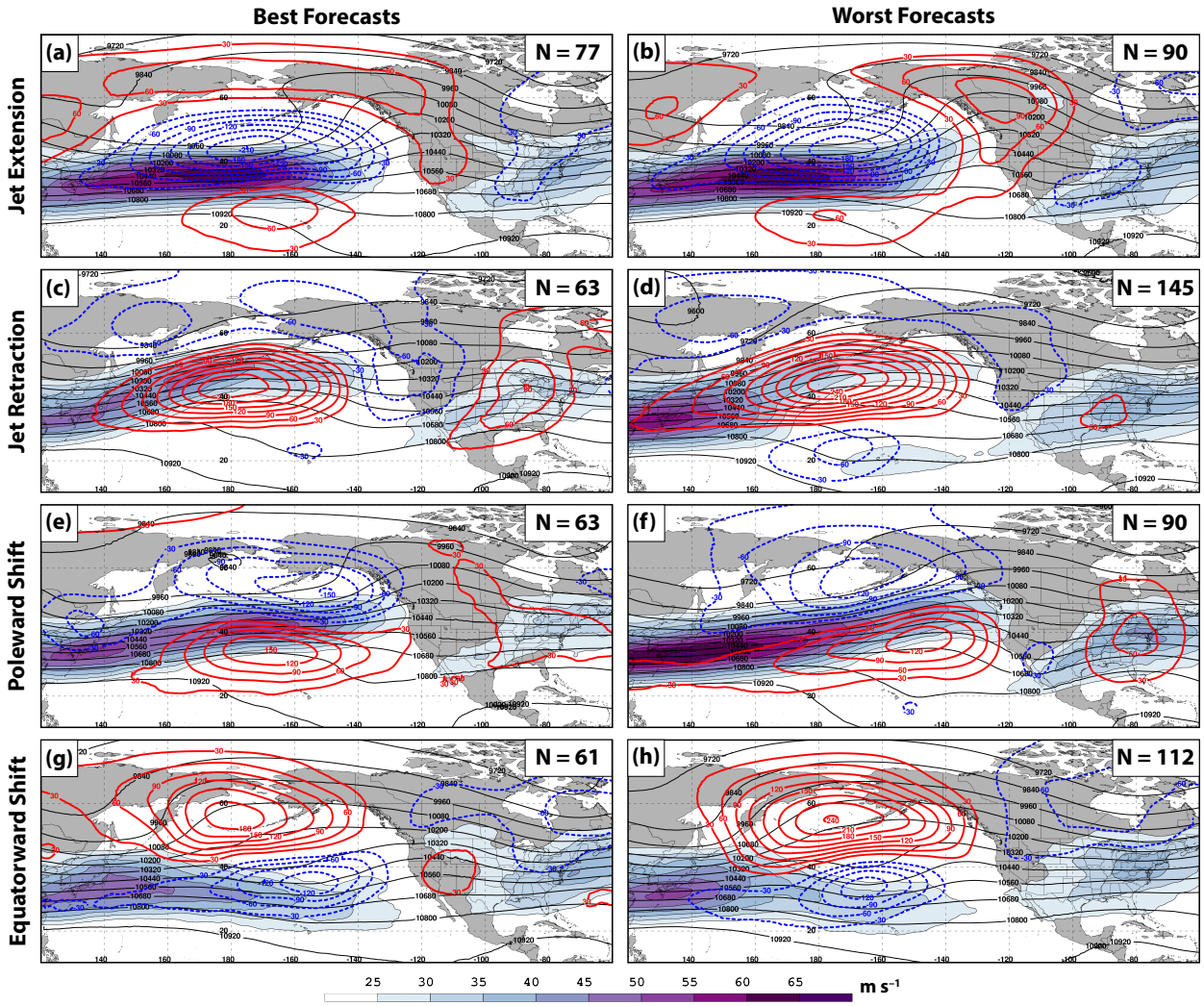

FIG. 13. Composite mean 250-hPa wind speed in m s^{-1} is shaded in the fill pattern, 250-hPa geopotential height is contoured in black every 120 m, and 250-hPa geopotential height anomalies are contoured in solid red and dashed blue every 30 m for positive and negative values, respectively, at the time a (a) best and (b) worst NPJ Phase Diagram forecast are initialized during a jet extension. (c),(d) As in (a),(b), but for those forecasts that are initialized during a jet retraction. (e),(f) As in (a),(b), but for those forecasts that are initialized during a poleward shift. (g),(h) As in (a),(b), but for those forecasts that are initialized during an equatorward shift. The quantities in the top right corner of every panel indicate the number of cases included in each composite.

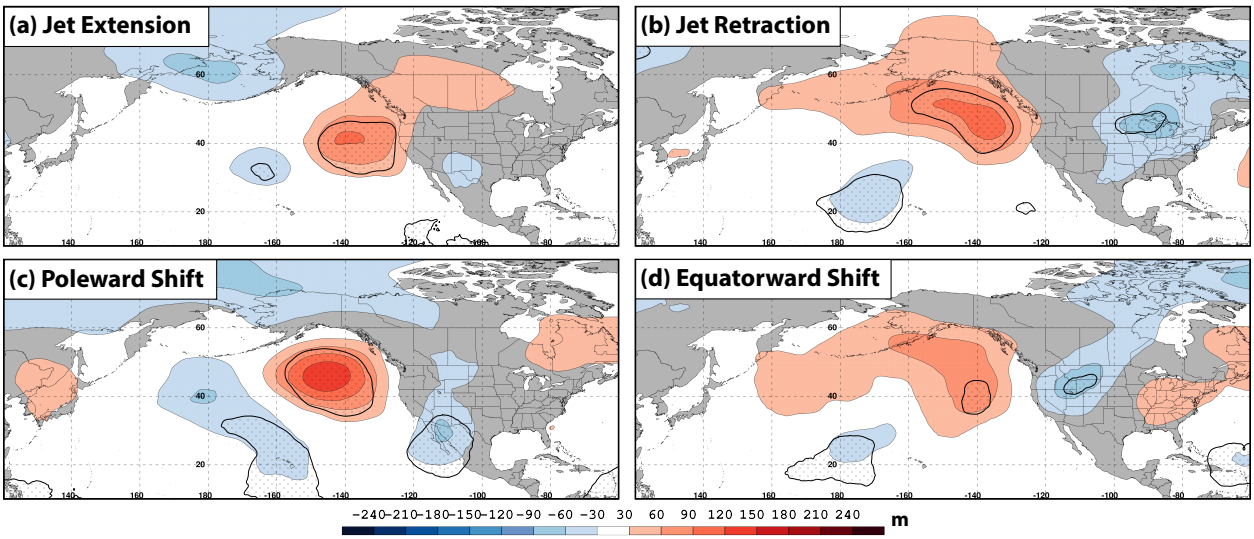

FIG. 14. (a) The difference between the 250-hPa geopotential height anomalies associated with a worst and best NPJ Phase Diagram forecast at the time of forecast initialization during a jet extension is shaded every 30 m in the fill pattern. (b) As in (a), but during a jet retraction. (c) As in (a), but during a poleward shift. (d) As in (a), but during an equatorward shift. Statistically significant differences in geopotential height anomalies at the 99% confidence level are stippled in all panels.

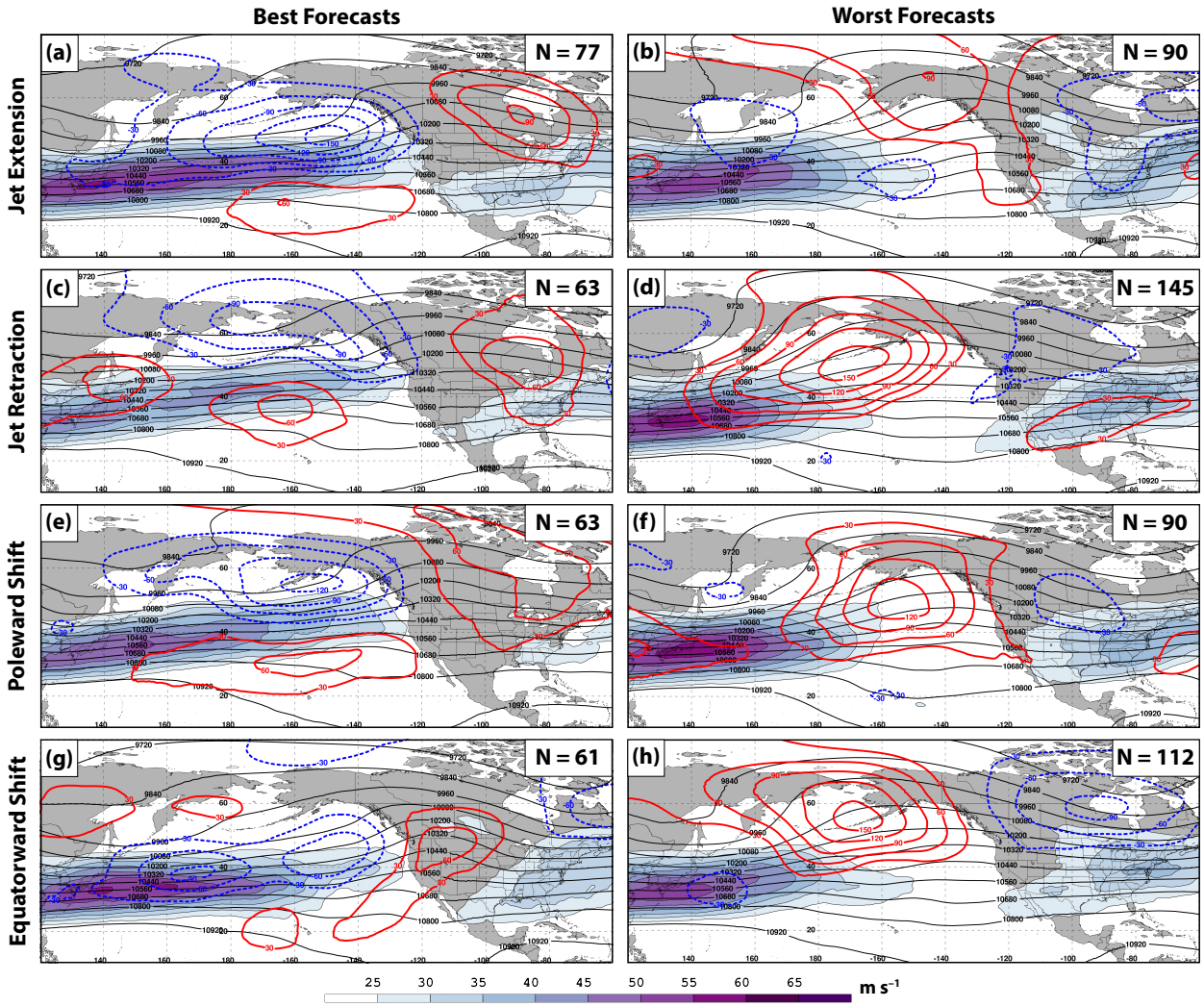

FIG. 15. As in Fig. 13, but for the composite 250-hPa flow patterns 192 h following the initialization of a best and worst NPJ Phase Diagram forecast.

1234

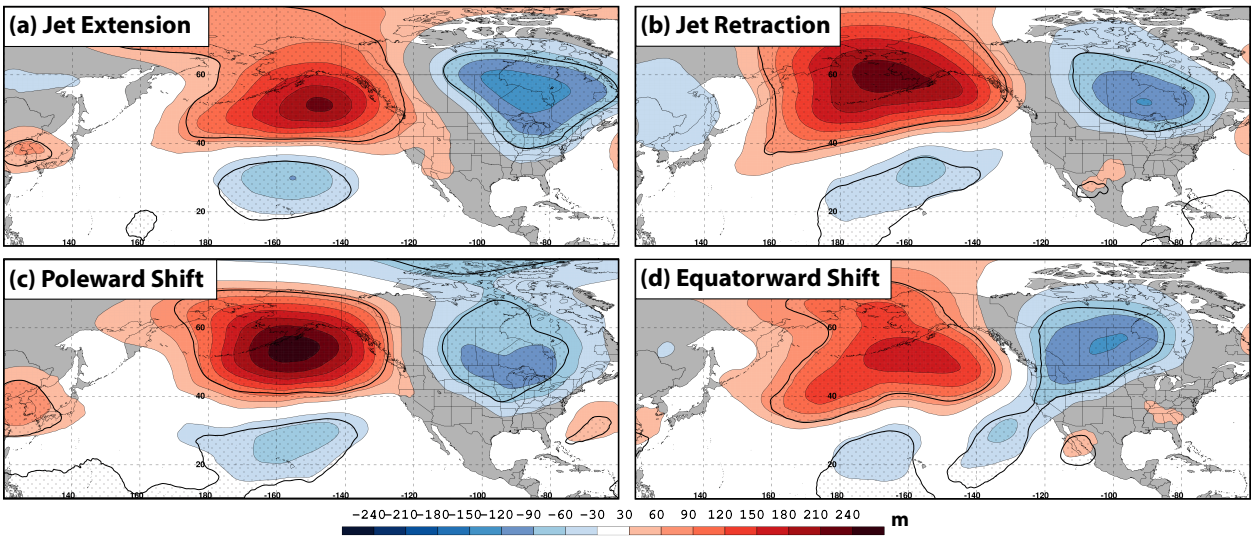

1235

1236 FIG. 16. As in Fig. 14, but for the composite difference between 250-hPa geopotential height
1237 anomalies 192 h following the initialization of a worst and best NPJ Phase Diagram forecast.
1238